Appl. Math. Mech. -Engl. Ed., **44**(8), 1241–1262 (2023)

APPLIED MATHEMATICS AND MECHANICS (ENGLISH EDITION)

https://doi.org/10.1007/s10483-023-3015-7

Flexural-wave-generation using a phononic crystal with a piezoelectric defect*

S. H. JO[1,†], D. LEE[2]

1. Department of Mechanical, Robotics, and Energy Engineering, Dongguk University, Seoul 04620, Republic of Korea;
2. Department of Mechanical Engineering, Seoul National University, Seoul 08826, Republic of Korea

(Received Mar. 2, 2023 / Revised May 26, 2023)

Abstract This paper proposes a method to amplify the performance of a flexural-wave-generation system by utilizing the energy-localization characteristics of a phononic crystal (PnC) with a piezoelectric defect and an analytical approach that accelerates the predictions of such wave-generation performance. The proposed analytical model is based on the Euler-Bernoulli beam theory. The proposed analytical approach, inspired by the transfer matrix and S-parameter methods, is used to perform band-structure and time-harmonic analyses. A comparison of the results of the proposed approach with those of the finite element method validates the high predictive capability and time efficiency of the proposed model. A case study is explored; the results demonstrate an almost ten-fold amplification of the velocity amplitudes of flexural waves leaving at a defect-band frequency, compared with a system without the PnC. Moreover, design guidelines for piezoelectric-defect-introduced PnCs are provided by analyzing the changes in wave-generation performance that arise depending on the defect location.

Key words phononic crystal (PnC), defect, wave-generation, flexural wave, analytical model

Chinese Library Classification O328, O346
2010 Mathematics Subject Classification 34A25, 81U15, 82C21

1 Introduction

Phononic crystals (PnCs), in which artificially designed unit cells are periodically arranged, have received significant research attention in recent years; the resulting work has dramatically expanded the boundaries of technology for manipulating the flow (e.g., amount and direction) of elastic wave energy[1–4]. One emerging research topic is the spatial localization and quantitative amplification of wave energy in a desired region via defect-introduced PnCs[5–8]. The periodic

* Citation: JO, S. H. and LEE, D. Flexural-wave-generation using a phononic crystal with a piezoelectric defect. *Applied Mathematics and Mechanics* (*English Edition*), **44**(8), 1241–1262 (2023) https://doi.org/10.1007/s10483-023-3015-7

† Corresponding author, E-mail: soohojo@dgu.ac.kr

Project supported by the Basic Science Research Program through the National Research Foundation of Korea, funded by the Ministry of Education (No. 2022R1I1A1A0105640611)

nature of a defect-free PnC contributes to the creation of Bragg-scattering-based phononic band gaps in its dispersion relationships (i.e., frequency versus wavenumber)[9–10]. Here and hereafter, when using the term 'defect', we envisage an engineering circumstance in which a structure with different geometric values and/or materials is used to replace a unit cell intentionally. When a defect is introduced, one or more passbands form within the phononic band gaps, which are called defect bands, with slopes close to zero. Defect bands appear to be tightly sandwiched in the separated band gaps. A previous study has shown that the band-gap feature of some unit cells that encloses the defect induces hypothetical, fixed-end boundary conditions due to evanescent waves; further, it brings about a mechanically resonating motion from the defect, called the defect-mode shape, at each frequency of the defect bands[11]. These intriguing properties facilitate a high-density concentration of elastic wave energy inside and near the defect.

Many engineers have devoted research effort to devising and producing valuable devices that harness such defect-mode-enabled energy-amplification characteristics. Instead of relying solely on traditional defect-introduced PnCs, the most recent research focus has been on intelligent-defect-introduced PnCs; these approaches keep practicality in mind by attaching intelligent materials to a defect or unit cell[12–13] or by imposing intelligent materials as a defect[14–15]. In general, the previous works that involve incorporating piezoelectric materials into the design stage of defect-introduced PnCs have offered particularly compelling results to move the related research forward[16–19]. The use of piezoelectric materials has several merits, including their quick response to external stimuli, versatility in fabrication, and their wide range of available frequencies[20]. Examples of applications of piezoelectric-defect-introduced PnCs include (i) energy harvesters or ultrasonic sensors that amplify the output electric energy generated by the piezoelectric elements when subjected to input elastic waves and (ii) ultrasonic transducers that amplify the output elastic waves generated when subjected to input electric energy.

The successful implementation of energy harvesters and ultrasonic sensors stems from the direct piezoelectric effect (from mechanical energy to electric energy). Attractive topics in this field cover three areas: (i) developing analytical or numerical models to predict the amount of electric power amplification[21–22], (ii) conducting experimental demonstrations for one- or two-dimensional PnCs[23–24], and (iii) advancing structural designs or electric circuit configurations to enhance electric power[25–26]. Unfortunately, research related to the development of ultrasonic transducers is only in its infancy. The slow progress of this field originates from the fact that most preliminary studies on defect-free or defect-introduced PnCs presume a situation where elastic waves are incident. As a groundbreaking paradigm shift, research into the idea of generating elastic waves using the converse piezoelectric effect (from electric energy to mechanical energy) began in 2022. Scrutinizing the existing works, one area of research seeks to develop analytical models that explicitly predict the generation performance of elastic waves when single or double defects are imposed[27–28]; however, this approach is limited to longitudinal waves. For this approach, research on the generation of flexural waves with more complicated governing equations remains an unrevealed area.

Hence, the objectives of this study are as follows: (i) make an academic bridge between a one-dimensional PnC with a piezoelectric defect and a flexural-wave-generation system and (ii) develop an analytical model that defines the predictions of the output performance of such an approach. To retain compatibility with the previous approaches that were made under longitudinal waves[27–28], the wave-generation performance is divided into two categories: (i) defect bands that emerge in the phononic band gaps and the corresponding defect-mode shapes (used in band-structure analysis), and (ii) velocity amplitudes of outgoing waves and electric current for a unit input voltage (used in time-harmonic analysis). Starting from the basis of the Euler-Bernoulli beam theory, the proposed analytical model considers both the transfer-matrix and S-parameter methods in each type of analysis. The predictive capability of the proposed analytical model is validated through comparison with the numerical model (e.g.,

finite-element-based model), using a case study with manufacturable materials and geometric values. Finally, a comparative study on the change in wave-generation performance according to the defect location is carried out from a design point of view.

The remainder of this paper is structured as follows. Section 2 delineates the schematic configuration of a one-dimensional, flexural-wave-generation system. Sections 3 and 4 offer mathematical derivation and numerical validation, respectively, of the proposed analytical model for band-structure and time-harmonic analyses. Section 5 analyzes how the wave-generation performance varies with the defect location. Finally, Section 6 summarizes this work and describes follow-up studies that should be pursued as the next stepping stones for the development of PnC-incorporated wave-generation systems.

2 System configuration and description

Figure 1(a) shows a front view of a one-dimensional, flexural-wave-generation system constructed with a PnC, in which bimorph piezoelectric patches adhere to a defect. In this paper, such a defect is referred to as a piezoelectric defect. A piezoceramic material is used for the patches, and the rest of the structures are made of metal. A composite structure, defined as a unit cell, consists of light and dark gray beams with a rectangular cross-section of constant area. A periodic arrangement of N unit cells in the 1-axis builds a defect-free PnC. Then, one defect is put in the periodic structure by changing the length of the light gray beam that is positioned in the Hth unit cell. Two dark blue piezoelectric patches with identical geometric values are fully attached to the top and bottom surfaces of the defect. The term 'fully' means that their attachment area covers the entire defect region. A thin layer of brown electrodes is placed on the top and bottom of each patch. An engineering circumstance is considered where light gray

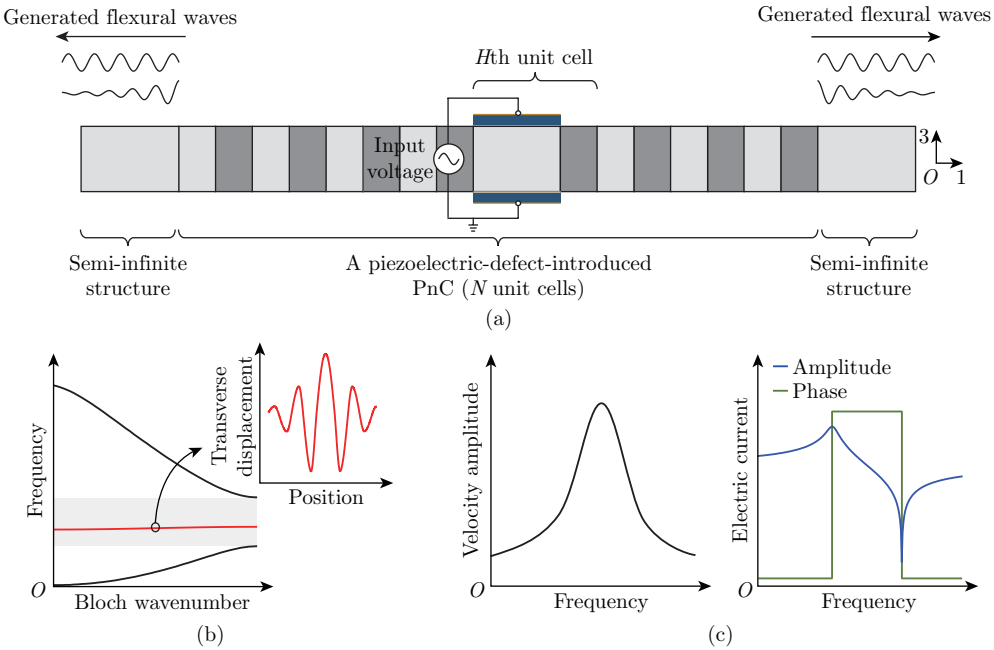

Fig. 1 An overview of this study: (a) integration of a flexural-wave-generation system and a PnC with a piezoelectric defect, (b) the prediction of phononic band gaps, defect bands, and corresponding defect-mode shapes in the band-structure analysis, and (c) the prediction of velocity amplitudes of generated flexural waves and electric current in the time-harmonic analysis (color online)

semi-infinite structures adhere to each end of the PnC. Generated flexural waves propagate outward through these structures. This semi-infinite setting prevents finite-condition-induced wave reflection, thus helping to analyze the intrinsic features of the defect-introduced PnC[28]. One previous study presents that the intrinsic properties of PnCs remain fixed regardless of finite or semi-infinite conditions through comparison with numerical analysis and experiment[29]. Here, perfect adhesion between all interfaces is presumed, which eliminates the need to consider delamination issues[30–31].

Symbols with the subscripts 'UL,' 'UD,' 'D,' 'P,' 'SL,' and 'SR' indicate the physical properties, respectively, of the light and dark gray beams in the unit cells, the light gray beam (defect), one piezoelectric patch in the piezoelectric defect, and the left and right semi-infinite structures. The assumption of complete attachment makes the defect and bimorph patches mechanically equivalent to one homogenized beam. In this regard, symbols with the subscript 'PD' correspond to their shared or homogenized characteristics. For geometric parameters, the symbols d and h denote the length and height, respectively. The lattice constant d_{Unit} of the unit cell is $d_{\mathrm{UL}} + d_{\mathrm{UD}}$. The total length d_{PnC} of the PnC is $(N-1)d_{\mathrm{Unit}} + d_{\mathrm{PD}} + d_{\mathrm{UD}}$. Other than the patches, the height of each structure is commonly denoted by h_{PnC}. Similarly, the symbol b_{PnC} denotes the width of the overall PnC. Of note, the length should be sufficiently greater than the height to comply with several assumptions of the Euler-Bernoulli beam theory[32–33]. In terms of the material properties, the symbols ρ and Y represent the mass density and Young's modulus of the metallic structures, respectively. The symbols c_{11}^{E}, ε_{33}^{S}, and e_{31} for the patches represent the 1-axial elastic modulus at a constant electric field E, the 3-axial dielectric permittivity at a constant strain field S, and the piezoelectric coupling coefficient, respectively.

An external input voltage source $V(t)$ induces the 3-axial electric polarization within the patches through electrical wires connected to the top patch's upper surface and the bottom patch's lower surface. From this viewpoint, the electrical configuration of the patches falls in the series connection. Unlike the case of longitudinal waves, it is worth pointing out that each poling direction in the patches is opposite. Hence, the different signs of their piezoelectric coupling coefficients result in opposing 1-axial mechanical deformations (i.e., elongation versus compression) of each patch in response to the identical 3-axial electric field[34–35]. This is the basic principle by which flexural waves are generated via the 31-mode converse piezoelectric effect. This is analogous to general piezoelectric actuators for transverse vibrations[36–37].

Unlike conventional, flexural-wave-generation systems where patches are directly attached to one homogeneous and infinite structure, flexural waves initially generated by the piezoelectric patches repeatedly undergo scattering (i.e., partial reflection and transmittance) at each interface between neighboring beams since the present PnC-integrated system consists of multiple beams with different mechanical impedances. When enough time passes to make the dynamic behaviors converge to a steady state, the flexural waves of interest finally propagate through the semi-infinite structures. Here, the target physical quantities are classified into two categories. The first category in Fig. 1(b) is, in the absence of a unit input voltage, a defect band that emerges in a phononic band gap and the corresponding defect-mode shape in the band-structure analysis. The other category in Fig. 1(c) is, in the presence of a unit input voltage, a velocity amplitude of outgoing waves and an electric current (e.g., its amplitude and phase) that are generated in the time-harmonic analysis.

3 The proposed analytical model under flexural waves

3.1 Derivation of governing equations and corresponding solutions

The Cartesian coordinates in the 1- and 3-axes are represented in terms of x and z, respectively. Recall that the proposed model is based on the Euler-Bernoulli beam theory. The transverse displacement and internal bending moment at an arbitrary space x and time t are denoted as $W(x,t)$ and $M(x,t)$, respectively. Newton's second law expresses the partial differ-

ential equation that governs the transverse motions of the piezoelectric defect as

$$b_{\mathrm{PnC}}(\rho_{\mathrm{D}}h_{\mathrm{PnC}}+2\rho_{\mathrm{P}}h_{\mathrm{P}})\frac{\partial^2 W_{\mathrm{PD}}(x_{\mathrm{PD}},t)}{\partial t^2}=\frac{\partial^2 M_{\mathrm{PD}}(x_{\mathrm{PD}},t)}{\partial x_{\mathrm{PD}}^2}, \tag{1}$$

where the internal bending moment $M_{\mathrm{PD}}(x_{\mathrm{PD}},t)$ is given by

$$M_{\mathrm{PD}}(x_{\mathrm{PD}},t)=b_{\mathrm{PnC}}\Big(\int_{z_{\mathrm{D}}} z_{\mathrm{D}}T_{\mathrm{D}}(x_{\mathrm{PD}},z_{\mathrm{D}},t)\mathrm{d}z_{\mathrm{D}}+\int_{z_{\mathrm{P}}} z_{\mathrm{P}}T_{\mathrm{P}}(x_{\mathrm{PD}},z_{\mathrm{P}},t)\mathrm{d}z_{\mathrm{P}}\Big), \tag{2}$$

where $z_{\mathrm{D}}\in(-h_{\mathrm{PnC}}/2,h_{\mathrm{PnC}}/2)$ and $z_{\mathrm{P}}\in(-h_{\mathrm{PnC}}/2-h_{\mathrm{P}},-h_{\mathrm{PnC}}/2)\cup(h_{\mathrm{PnC}}/2,h_{\mathrm{PnC}}/2+h_{\mathrm{P}})$. Here, $T_{\mathrm{D}}(x_{\mathrm{PD}},z_{\mathrm{D}},t)$ and $T_{\mathrm{P}}(x_{\mathrm{PD}},z_{\mathrm{P}},t)$ stand for the normal stresses of the defect and bimorph patches along the 1-axis, respectively. In accordance with the Euler-Bernoulli beam theory, the remaining stresses are assumed to vanish throughout the interior of the piezoelectric defect. According to the small deformation theory under flexural waves, the linear constitutive relations express the normal stresses $T_{\mathrm{D}}(x_{\mathrm{PD}},z_{\mathrm{D}},t)$ and $T_{\mathrm{P}}(x_{\mathrm{PD}},z_{\mathrm{P}},t)$ as[38–39]

$$\begin{cases} T_{\mathrm{D}}(x_{\mathrm{PD}},z_{\mathrm{D}},t)=-z_{\mathrm{D}}Y_{\mathrm{D}}\dfrac{\partial^2 W_{\mathrm{PD}}(x_{\mathrm{PD}},t)}{\partial x_{\mathrm{PD}}^2}, \\ T_{\mathrm{P}}(x_{\mathrm{PD}},z_{\mathrm{P}},t)=-z_{\mathrm{P}}c_{11}^{E}\dfrac{\partial^2 W_{\mathrm{PD}}(x_{\mathrm{PD}},t)}{\partial x_{\mathrm{PD}}^2}+\mathrm{sgn}(z_{\mathrm{P}})e_{31}E_{\mathrm{P}}(x_{\mathrm{PD}},z_{\mathrm{P}},t), \end{cases} \tag{3}$$

where $\mathrm{sgn}(z)$ indicates the sign of z. When a piezoelectric patch is sufficiently thin, an electric field that is the negative, spatial derivative (gradient) of the electric potential is assumed to be uniform throughout its interior[40–41]. Here, the series connection makes the difference between the electric potentials of the top patch's upper surface and the bottom patch's lower surface equal to the input voltage $V(t)$. Therefore, the 3-axial electric field $E_{\mathrm{P}}(x_{\mathrm{PD}},z_{\mathrm{P}},t)$ can be expressed as

$$E_{\mathrm{P}}(x_{\mathrm{PD}},z_{\mathrm{P}},t)=-\frac{V(t)\Pi(x_{\mathrm{PD}};0,d_{\mathrm{PD}})}{2h_{\mathrm{P}}}, \tag{4}$$

where the electric fields in the remaining axes are assumed to be negligible. The boxcar function $\Pi(x;a,b)$ mathematically equals $H(x-a)-H(x-b)$, where $H(x)$ stands for the Heaviside step function and $b\geqslant a$. The use of this boxcar function $\Pi(x_{\mathrm{PD}};0,d_{\mathrm{PD}})$ presents the attachment domain of the piezoelectric patches and limits the generation of the electric field within the patches. Previous works that handle piezoelectric effects use this mathematical technique to avoid removing the electric field-related terms in the differentiation processes[34–35,40–41]. In particular, the previous analytical models with this technique under longitudinal waves exhibit good agreement with the results of the finite element method[27–28]. Finally, inserting Eqs. (2)–(4) into Eq. (1) rewrites the mechanical equation of transverse motions as

$$\begin{aligned} &(\rho A)_{\mathrm{PD}}\frac{\partial^2 W_{\mathrm{PD}}(x_{\mathrm{PD}},t)}{\partial t^2}+(YJ)_{\mathrm{PD}}\frac{\partial^4 W_{\mathrm{PD}}(x_{\mathrm{PD}},t)}{\partial x_{\mathrm{PD}}^4} \\ &=\vartheta_{\mathrm{P}}V(t)\Big(\frac{\mathrm{d}\delta(x_{\mathrm{PD}})}{\mathrm{d}x_{\mathrm{PD}}}-\frac{\mathrm{d}\delta(x_{\mathrm{PD}}-d_{\mathrm{PD}})}{\mathrm{d}x_{\mathrm{PD}}}\Big), \end{aligned} \tag{5}$$

where the Dirac delta function $\delta(x)$ is the derivative of the Heaviside function $H(x)$. $(\rho A)_{\mathrm{PD}}$ and $(YJ)_{\mathrm{PD}}$ denote the equivalent mass per unit length and bending stiffness, respectively, of the piezoelectric defect. ϑ_{P} denotes the electroelastic coupling coefficient of the patches. These quantities are calculated by

$$\begin{cases} (\rho A)_{\mathrm{PD}}=b_{\mathrm{PnC}}(\rho_{\mathrm{D}}h_{\mathrm{PnC}}+2\rho_{\mathrm{P}}h_{\mathrm{P}}), \\ (YJ)_{\mathrm{PD}}=b_{\mathrm{PnC}}\Big(\dfrac{Y_{\mathrm{D}}h_{\mathrm{PnC}}^3}{12}+\dfrac{2c_{11}^{E}}{3}\Big(\Big(\dfrac{h_{\mathrm{PnC}}}{2}+h_{\mathrm{P}}\Big)^3-\Big(\dfrac{h_{\mathrm{PnC}}}{2}\Big)^3\Big)\Big), \\ \vartheta_{\mathrm{P}}=b_{\mathrm{PnC}}e_{31}\Big(\dfrac{h_{\mathrm{PnC}}+h_{\mathrm{P}}}{2}\Big). \end{cases} \tag{6}$$

At the same time, the combination of the electroelastic coupling in bimorph patches and the electrical polarization induced by the input voltage produces an output electric current. Due to the series connection of patches with the same specifications and configuration, the total electric current is equal to the electric current generated by each patch. Gauss's law expresses the output electric current $I(t)$ as

$$I(t) = \frac{\mathrm{d}}{\mathrm{d}t}\Big(b_{\mathrm{PnC}} \int_0^{d_{\mathrm{PD}}} D_{\mathrm{P}}\Big(x_{\mathrm{PD}}, \frac{h_{\mathrm{PnC}} + h_{\mathrm{P}}}{2}, t\Big)\mathrm{d}x_{\mathrm{PD}}\Big), \tag{7}$$

where the constitutive equation of linear piezoelectricity specifies the electric displacement $D_{\mathrm{P}}(x_{\mathrm{PD}}, z_{\mathrm{P}}, t)$ as[38–39]

$$D_{\mathrm{P}}(x_{\mathrm{PD}}, z_{\mathrm{P}}, t) = \varepsilon_{33}^{S} E_{\mathrm{P}}(x_{\mathrm{PD}}, z_{\mathrm{P}}, t) - \mathrm{sgn}(z_{\mathrm{P}}) z_{\mathrm{P}} e_{31} \frac{\partial^2 W_{\mathrm{PD}}(x_{\mathrm{PD}}, t)}{\partial x_{\mathrm{PD}}^2}. \tag{8}$$

Here, the normal strain at $z_{\mathrm{P}} = (h_{\mathrm{PnC}} + h_{\mathrm{P}})/2$ is considered as an averaging value. Finally, inserting Eq. (8) into Eq. (7) rewrites the electrical circuit equation as

$$I(t) = -\frac{C_{\mathrm{P}}}{2}\frac{\mathrm{d}V(t)}{\mathrm{d}t} - \vartheta_{\mathrm{P}}\Big(\frac{\partial^2 W_{\mathrm{PD}}(x_{\mathrm{PD}}, t)}{\partial x_{\mathrm{PD}} \partial t}\Big|_{x_{\mathrm{PD}}=d_{\mathrm{PD}}} - \frac{\partial^2 W_{\mathrm{PD}}(x_{\mathrm{PD}}, t)}{\partial x_{\mathrm{PD}} \partial t}\Big|_{x_{\mathrm{PD}}=0}\Big), \tag{9}$$

where C_{P} denotes the capacitance of one patch, which is calculated by

$$C_{\mathrm{P}} = \frac{\epsilon_{33}^{S} b_{\mathrm{PnC}} d_{\mathrm{PD}}}{h_{\mathrm{P}}}. \tag{10}$$

Parallel to the previous analytical models for longitudinal-wave-generation, it is important to note two highlighted items in this work. First, the mechanical equation of transverse motions for the piezoelectric defect in Eq. (5) considers the inertia, bending stiffness, and electroelastic coupling of the piezoelectric patches that are listed in Eq. (6). Second, the electrical circuit equation in Eq. (9) considers non-uniform strain distributions in the electroelastic coupling term. However, two distinctive points also exist. First, the mechanical equation of transverse motions lies in the fourth-order partial differential equations. Further, rather than the Dirac delta functions themselves, the electroelastic coupling term in Eq. (5) is expressed in terms of its differential form. Second, in this case, the difference in transverse slopes at the ends of the piezoelectric-patch-attached defect contributes to the electroelastic coupling term in Eq. (9). On the other hand, the difference in the longitudinal displacements is of concern in the longitudinal wave studies. Beyond simply switching the wave types of interest, these notable issues set our study apart from the previous works.

When the wave-generation system undergoes harmonic motions over time, the output transverse displacement $W_{\mathrm{PD}}(x_{\mathrm{PD}}, t)$, electric current $I(t)$, and input voltage $V(t)$ can be rewritten as $W_{\mathrm{PD}}(x)\exp(-\mathrm{j}\omega t)$, $I(\omega)\exp(-\mathrm{j}\omega t)$, and $V(\omega)\exp(-\mathrm{j}\omega t)$, respectively. These harmonic expressions simplify each governing equation in Eqs. (5) and (9), respectively, in terms of ordinary differential equations as

$$(YJ)_{\mathrm{PD}} \frac{\mathrm{d}^4 W_{\mathrm{PD}}(x_{\mathrm{PD}})}{\mathrm{d}x_{\mathrm{PD}}^4} - \omega^2 (\rho A)_{\mathrm{PD}} W_{\mathrm{PD}}(x_{\mathrm{PD}}) = \vartheta_{\mathrm{P}} V(\omega)\Big(\frac{\mathrm{d}\delta(x_{\mathrm{PD}})}{\mathrm{d}x_{\mathrm{PD}}} - \frac{\mathrm{d}\delta(x_{\mathrm{PD}} - d_{\mathrm{PD}})}{\mathrm{d}x_{\mathrm{PD}}}\Big), \tag{11}$$

$$I(\omega) = \frac{\mathrm{j}\omega C_{\mathrm{P}}}{2} V(\omega) + \mathrm{j}\omega\vartheta_{\mathrm{P}}\Big(\frac{\mathrm{d}W_{\mathrm{PD}}(x_{\mathrm{PD}})}{\mathrm{d}x_{\mathrm{PD}}}\Big|_{x_{\mathrm{PD}}=d_{\mathrm{PD}}} - \frac{\mathrm{d}W_{\mathrm{PD}}(x_{\mathrm{PD}})}{\mathrm{d}x_{\mathrm{PD}}}\Big|_{x_{\mathrm{PD}}=0}\Big). \tag{12}$$

A homogeneous solution $W_{\mathrm{PD}}^{\mathrm{H}}(x_{\mathrm{PD}})$ to Eq. (11) is well known as the linear combination of hyperbolic ($\sinh(kx)$ and $\cosh(kx)$) and trigonometric ($\sin(kx)$ and $\cos(kx)$) functions. Its non-homogeneous solution $W_{\mathrm{PD}}^{\mathrm{NH}}(x_{\mathrm{PD}})$ can be obtained with the help of Green's function. Recall that

the electroelastic coupling term is the sum of two derivatives of Dirac delta functions $\delta(x_{\mathrm{PD}})$ and $\delta(x_{\mathrm{PD}} - d_{\mathrm{PD}})$. Physically, $\delta(x - x_0)$ means the concentrated unit transverse force that is excited at $x = x_0$ in wave equations, and the corresponding wave solution is called Green's function[42–43]. Hence, multiplying the coefficient $\vartheta_{\mathrm{P}} V(\omega)$ but summing the two derivatives of the corresponding Green's functions yields the non-homogeneous solution. Consequently, the general solution of the transverse displacement field $W_{\mathrm{PD}}(x_{\mathrm{PD}})$ within the piezoelectric defect becomes

$$\begin{cases} W_{\mathrm{PD}}(x_{\mathrm{PD}}) = W_{\mathrm{PD}}^{\mathrm{H}}(x_{\mathrm{PD}}) + W_{\mathrm{PD}}^{\mathrm{NH}}(x_{\mathrm{PD}}), \\ W_{\mathrm{PD}}^{\mathrm{H}}(x_{\mathrm{PD}}) = o_{\mathrm{PD}} O(k_{\mathrm{PD}} x_{\mathrm{PD}}) + p_{\mathrm{PD}} P(k_{\mathrm{PD}} x_{\mathrm{PD}}) + q_{\mathrm{PD}} Q(k_{\mathrm{PD}} x_{\mathrm{PD}}) + r_{\mathrm{PD}} R(k_{\mathrm{PD}} x_{\mathrm{PD}}), \\ W_{\mathrm{PD}}^{\mathrm{NH}}(x_{\mathrm{PD}}) = \dfrac{\vartheta_{\mathrm{P}} V(\omega)}{4(YJ)_{\mathrm{PD}} k_{\mathrm{PD}}^2} ((-1+\mathrm{j})(R(k_{\mathrm{PD}} x_{\mathrm{PD}}) + R(k_{\mathrm{PD}}(d_{\mathrm{PD}} - x_{\mathrm{PD}}))) \\ \qquad\qquad + (-1-\mathrm{j})(P(k_{\mathrm{PD}} x_{\mathrm{PD}}) + P(k_{\mathrm{PD}}(d_{\mathrm{PD}} - x_{\mathrm{PD}}))) \\ \qquad\qquad + 2(Q(k_{\mathrm{PD}} x_{\mathrm{PD}}) + Q(k_{\mathrm{PD}}(d_{\mathrm{PD}} - x_{\mathrm{PD}})))), \end{cases} \tag{13}$$

where its wavenumber k_{PD} is calculated by

$$k_{\mathrm{PD}} = \sqrt[4]{\frac{\omega^2 (\rho A)_{\mathrm{PD}}}{(YJ)_{\mathrm{PD}}}}. \tag{14}$$

$O(kx)$, $P(kx)$, $Q(kx)$, and $R(kx)$ are combinations of the hyperbolic and trigonometric functions, which are defined, respectively,

$$\begin{cases} O(kx) = \dfrac{1}{2}\left(\cosh(kx) + \cos(kx)\right), \\ P(kx) = \dfrac{1}{2}(\sinh(kx) + \sin(kx)), \\ Q(kx) = \dfrac{1}{2}(\cosh(kx) - \cos(kx)), \\ R(kx) = \dfrac{1}{2}(\sinh(kx) - \sin(kx)t). \end{cases} \tag{15}$$

Inserting Eq. (13) into Eq. (12) rewrites the output electric current $I(\omega)$ as

$$\begin{aligned} I(\omega) =& \mathrm{j}\omega\vartheta_{\mathrm{P}} k_{\mathrm{PD}} \left(o_{\mathrm{PD}} R(k_{\mathrm{PD}} d_{\mathrm{PD}}) + p_{\mathrm{PD}}(O(k_{\mathrm{PD}} d_{\mathrm{PD}}) - 1) + q_{\mathrm{PD}} P(k_{\mathrm{PD}} d_{\mathrm{PD}}) + r_{\mathrm{PD}} Q(k_{\mathrm{PD}} d_{\mathrm{PD}})\right) \\ &+ \frac{\mathrm{j}\omega\vartheta_{\mathrm{P}}^2 V(\omega)}{2(YJ)_{\mathrm{PD}} k_{\mathrm{PD}}} ((-1+\mathrm{j}) Q(k_{\mathrm{PD}} d_{\mathrm{PD}}) + (-1-\mathrm{j})(O(k_{\mathrm{PD}} d_{\mathrm{PD}}) - 1) \\ &+ 2P(k_{\mathrm{PD}} d_{\mathrm{PD}})) + \frac{\mathrm{j}\omega C_{\mathrm{P}} V(\omega)}{2}. \end{aligned} \tag{16}$$

Transverse displacement fields of the remaining structures in the absence of the bimorph patches can be readily obtained by removing the electroelastic coupling-related term (i.e., the last term on the right-hand side of Eq. (13)). Naturally, the generation of electric current does not occur in Eq. (16). In addition, setting the height of the patches in Eq. (6) as zero gives information on their mass per unit length and bending stiffness. Hence, their transverse displacement field becomes

$$W_i(x_i) = o_i O(k_i x_i) + p_i P(k_i x_i) + q_i Q(k_i x_i) + r_i R(k_i x_i), \tag{17}$$

where $i \in \{\mathrm{UL}, \mathrm{UD}, \mathrm{SL}, \mathrm{SR}\}$. The corresponding wavenumber k_i is calculated by

$$k_i = \sqrt[4]{\frac{12\omega^2 \rho_i}{Y_i h_{\mathrm{PnC}}^2}}. \tag{18}$$

Here, o, p, q, and r are the unknown transverse displacement coefficients in Eqs. (13), (16), and (18). The following two subsections, Subsections 3.2 and 3.3, deal with the specifications of these coefficients in the band-structure and time-harmonic analyses, respectively.

3.2 Prediction of defect bands and their defect-mode shapes within phononic band gaps

A band structure is the computational product of a typical eigenvalue problem in wave engineering. Band-structure analysis in waves has the same physical meaning as modal analysis in vibrations. This work focuses on the transfer-matrix method, from various methods, such as the finite element method[44–45] and the plane-wave-expansion method[46–47]. The transfer-matrix method, which is specialized for one-dimensional engineering problems, is based on mathematical solutions to wave equations. The transfer matrix $\boldsymbol{TM}$ refers to one matrix that quantifies the direct relationship between two vectors of specific physical quantities at the left and right ends of a structure[48–49]. Unlike longitudinal waves, the fourth-order partial differential equation in Eq. (11) results in a 4×4 transfer matrix. In this subsection, the physical quantities of interest are the transverse displacement, slope, internal bending moment, and internal shear force. In addition, this subsection focuses only on the unit cell or defect-introduced PnC since the band structure aims to reveal the inherent characteristics of defect-free or defect-introduced PnCs. In other words, the existence of semi-infinite structures is ignored.

Since applying an input voltage to piezoelectric patches is equivalent to applying an external, dynamic force to one mechanical system, this subsection considers the absence of the input voltage (i.e., $V(\omega) = 0$). In other words, the electroelastic coupling terms in Eqs. (13) and (16) are negligible. This setting helps to derive the harmonic expressions of the slope $S^{\mathrm{BS}}(x)$, internal bending moment $M^{\mathrm{BS}}(x)$, and internal shear force $F^{\mathrm{BS}}(x)$ as

$$\begin{cases} S_{\mathrm{PD}}^{\mathrm{BS}}(x_{\mathrm{PD}}) = \dfrac{\mathrm{d}W_{\mathrm{PD}}^{\mathrm{BS}}(x_{\mathrm{PD}}|V(\omega)=0)}{\mathrm{d}x_{\mathrm{PD}}}, \\ S_i^{\mathrm{BS}}(x_i) = \dfrac{\mathrm{d}W_i^{\mathrm{BS}}(x_i)}{\mathrm{d}x_i}, \\ M_{\mathrm{PD}}^{\mathrm{BS}}(x_{\mathrm{PD}}) = -(YJ)_{\mathrm{PD}} \dfrac{\mathrm{d}^2 W_{\mathrm{PD}}^{\mathrm{BS}}(x_{\mathrm{PD}}|V(\omega)=0)}{\mathrm{d}x_{\mathrm{PD}}^2}, \\ M_i^{\mathrm{BS}}(x_i) = -\dfrac{Y_i b_{\mathrm{PnC}} h_{\mathrm{PnC}}^3}{12} \dfrac{\mathrm{d}^2 W_i^{\mathrm{BS}}(x_i)}{\mathrm{d}x_i^2}, \\ F_{\mathrm{PD}}^{\mathrm{BS}}(x_{\mathrm{PD}}) = (YJ)_{\mathrm{PD}} \dfrac{\mathrm{d}^3 W_{\mathrm{PD}}^{\mathrm{BS}}(x_{\mathrm{PD}}|V(\omega)=0)}{\mathrm{d}x_{\mathrm{PD}}^3}, \\ F_i^{\mathrm{BS}}(x_i) = \dfrac{Y_i b_{\mathrm{PnC}} h_{\mathrm{PnC}}^3}{12} \dfrac{\mathrm{d}^3 W_i^{\mathrm{BS}}(x_i)}{\mathrm{d}x_i^3}, \end{cases} \tag{19}$$

where the superscript 'BS' is the abbreviation of band-structure analysis. Due to the absence of the input voltage, the solution forms of $W_{\mathrm{PD}}^{\mathrm{BS}}(x_{\mathrm{PD}})$, $S_{\mathrm{PD}}^{\mathrm{BS}}(x_{\mathrm{PD}})$, $M_{\mathrm{PD}}^{\mathrm{BS}}(x_{\mathrm{PD}})$, and $F_{\mathrm{PD}}^{\mathrm{BS}}(x_{\mathrm{PD}})$ are the same as those of $W_i(x_i)$, $S_i(x_i)$, $M_i(x_i)$, and $F_i(x_i)$. Further, these field quantities are also the functions of the unknown transverse displacement coefficients o, p, q, and r. Hence, a 4×4 matrix $\boldsymbol{CM}^{\mathrm{BS}}$ is defined, which connects $(o\ \ p\ \ q\ \ r)^{\mathrm{T}}$ with $(W(x)\ \ S(x)\ \ M(x)\ \ F(x))^{\mathrm{T}}$ at an arbitrary point x. The superscript 'T' denotes the transposition of vectors or matrices. Symbols with the subscripts 'L' and 'R' stand for the left and right ends (i.e., $x = 0$ and d) of one structure. Then, $\boldsymbol{CM}_{\mathrm{L}}^{\mathrm{BS}}$ and $\boldsymbol{CM}_{\mathrm{R}}^{\mathrm{BS}}$ are given by

$$\begin{cases} (W_n(x_n)\ \ S_n(x_n)\ \ M_n(x_n)\ \ F_n(x_n))_{x_n=0}^{\mathrm{T}} = \boldsymbol{CM}_{n,\mathrm{L}}^{\mathrm{BS}}(o_n\ \ p_n\ \ q_n\ \ r_n)^{\mathrm{T}}, \\ (W_n(x_n)\ \ S_n(x_n)\ \ M_n(x_n)\ \ F_n(x_n))_{x_n=d_n}^{\mathrm{T}} = \boldsymbol{CM}_{n,\mathrm{R}}^{\mathrm{BS}}(o_n\ \ p_n\ \ q_n\ \ r_n)^{\mathrm{T}}, \end{cases} \tag{20}$$

where $n \in \{\mathrm{UL}, \mathrm{UD}, \mathrm{PD}\}$. Finally, the 4×4 transfer matrix $\boldsymbol{TM}^{\mathrm{BS}}$ under flexural waves becomes

$$\boldsymbol{TM}_n^{\mathrm{BS}} = \boldsymbol{CM}_{n,\mathrm{R}}^{\mathrm{BS}} (\boldsymbol{CM}_{n,\mathrm{L}}^{\mathrm{BS}})^{-1}. \tag{21}$$

One important assumption is that the mentioned field quantities are assumed to be continuous throughout the PnC. This implies that the continuity condition takes place for all interfaces where the materials of the beams are different. This setting helps to obtain the transfer matrices at the unit cell and piezoelectric-defect-introduced PnC levels. The transfer matrices $\boldsymbol{TM}_{\mathrm{Unit}}^{\mathrm{BS}}$ and $\boldsymbol{TM}_{\mathrm{PnC}}^{\mathrm{BS}}$ that relate the vectors of four physical quantities at their leftmost and rightmost sides of the unit cell and PnC become, respectively,

$$\begin{cases} \boldsymbol{TM}_{\mathrm{Unit}}^{\mathrm{BS}} = \boldsymbol{TM}_{\mathrm{UD}}^{\mathrm{BS}} \boldsymbol{TM}_{\mathrm{UL}}^{\mathrm{BS}}, \\ \boldsymbol{TM}_{\mathrm{PnC}}^{\mathrm{BS}} = \left(\boldsymbol{TM}_{\mathrm{Unit}}^{\mathrm{BS}}\right)^{N-H} \boldsymbol{TM}_{\mathrm{UD}}^{\mathrm{BS}} \boldsymbol{TM}_{\mathrm{PD}}^{\mathrm{BS}} \left(\boldsymbol{TM}_{\mathrm{Unit}}^{\mathrm{BS}}\right)^{H-1}. \end{cases} \tag{22}$$

In accordance with the supercell technique[50–51], when the Floquet-Bloch theorem applies the periodic boundary condition to these transfer matrices in Eq. (22), two eigenvalue problems are formulated as

$$\begin{cases} (\boldsymbol{TM}_{\mathrm{Unit}}^{\mathrm{BS}}(\omega_{\mathrm{Unit}}) - \exp(\mathrm{j} k_{\mathrm{Unit}}^{\mathrm{Bloch}} d_{\mathrm{Unit}}) \boldsymbol{I}_{4\times4})(W_{\mathrm{Unit}} \;\; S_{\mathrm{Unit}} \;\; M_{\mathrm{Unit}} \;\; F_{\mathrm{Unit}})_{\mathrm{Leftmost}}^{\mathrm{T}} = \boldsymbol{0}_{4\times1}, \\ (\boldsymbol{TM}_{\mathrm{PnC}}^{\mathrm{BS}}(\omega_{\mathrm{PnC}}) - \exp(\mathrm{j} k_{\mathrm{PnC}}^{\mathrm{Bloch}} d_{\mathrm{PnC}}) \boldsymbol{I}_{4\times4})(W_{\mathrm{PnC}} \;\; S_{\mathrm{PnC}} \;\; M_{\mathrm{PnC}} \;\; F_{\mathrm{PnC}})_{\mathrm{Leftmost}}^{\mathrm{T}} = \boldsymbol{0}_{4\times1}, \end{cases} \tag{23}$$

where $\boldsymbol{I}_{a\times a}$ is the $a \times a$ identity matrix, and $\boldsymbol{0}_{a\times b}$ is the $a \times b$ zero matrix. The subscript 'Leftmost' stands for the leftmost position of the given composite structures. Real-valued, normalized Bloch wavenumbers $k_{\mathrm{Unit}}^{\mathrm{Bloch}} d_{\mathrm{Unit}}$ and $k_{\mathrm{PnC}}^{\mathrm{Bloch}} d_{\mathrm{PnC}}$ lie in the first Brillouin zone that ranges from zero to π[50–51]. Numerical computation of a corresponding set of normalized Bloch wavenumbers (eigenvalues), for a given frequency range, that satisfy the characteristic equation in Eq. (23) enables the stipulation of each band structure of the unit cell (ω_{Unit} versus $k_{\mathrm{Unit}}^{\mathrm{Bloch}}$) or piezoelectric-defect-introduced PnC (ω_{PnC} versus $k_{\mathrm{PnC}}^{\mathrm{Bloch}}$). At the unit-cell level, the first equation in Eq. (23) determines the phononic band gaps where the frequency regimes do not correspond to Bloch wavenumbers. At the piezoelectric-defect-introduced PnC level, the second equation in Eq. (23) specifies defect-band frequencies that correspond to the Bloch wavenumber after reducing the frequency range of interest to phononic band gaps.

Furthermore, the eigenvalue problem for the piezoelectric-defect-introduced PnC yields a set of eigenvectors that corresponds to a set of defect-band frequencies. Recall that each eigenvector represents a vector of four physical quantities at the leftmost end of the PnC. Using the inverse matrix of $\boldsymbol{CM}_{\mathrm{L}}^{\mathrm{BS}}$, the first equation in Eq. (20) gives the values of the transverse displacement coefficients for the first beam and specifies its displacement field. Next, the multiplication of one transfer matrix $\boldsymbol{TM}^{\mathrm{BS}}$ in Eq. (21) and the computed eigenvector constitutes a vector of four physical quantities at the left end of the second beam. Hence, its displacement field can be determined in a similar manner. Finally, execution of this procedure for each beam step by step determines the transverse displacement field (called the defect-mode shape) of the piezoelectric-defect-introduced PnC.

3.3 Prediction of the velocity amplitudes of outgoing flexural waves and electric current

The main concern of the research described in this subsection is the prediction of the velocity amplitudes of outgoing waves and electric current (i.e., its amplitude and phase) in the presence of the input voltage. Additionally, unlike the band-structure analysis in Subsection 3.2, the existence of the semi-infinite structures is taken into account. In the time-harmonic analysis, a new vector is defined as $(W(x) \;\; S(x) \;\; M(x) \;\; F(x) \;\; V(\omega))^{\mathrm{T}}$. Note that the input voltage $V(\omega)$ is a given scalar value, while the remaining components are the functions of space x that need

to be computed. The expressions of the slope $S^{\mathrm{TH}}(x)$, internal bending moment $M^{\mathrm{TH}}(x)$, and internal shear force $F^{\mathrm{TH}}(x)$ are

$$\begin{cases} S_{\mathrm{PD}}^{\mathrm{TH}}(x_{\mathrm{PD}}) = \dfrac{\mathrm{d}W_{\mathrm{PD}}^{\mathrm{TH}}(x_{\mathrm{PD}}|V(\omega)\neq 0)}{\mathrm{d}x_{\mathrm{PD}}}, \\ S_i^{\mathrm{TH}}(x_i) = \dfrac{\mathrm{d}W_i^{\mathrm{TH}}(x_i)}{\mathrm{d}x_i}, \\ M_{\mathrm{PD}}^{\mathrm{TH}}(x_{\mathrm{PD}}) = -(YJ)_{\mathrm{PD}}\dfrac{\mathrm{d}^2W_{\mathrm{PD}}^{\mathrm{TH}}(x_{\mathrm{PD}}|V(\omega)\neq 0)}{\mathrm{d}x_{\mathrm{PD}}^2} + \vartheta_{\mathrm{P}}V(\omega), \\ M_i^{\mathrm{TH}}(x_i) = -\dfrac{Y_i b_{\mathrm{PnC}} h_{\mathrm{PnC}}^3}{12}\dfrac{\mathrm{d}^2W_i^{\mathrm{TH}}(x_i)}{\mathrm{d}x_i^2}, \\ F_{\mathrm{PD}}^{\mathrm{TH}}(x_{\mathrm{PD}}) = \displaystyle\int \omega^2(\rho A)_{\mathrm{PD}} W_{\mathrm{PD}}^{\mathrm{TH}}(x_{\mathrm{PD}}|V(\omega)\neq 0)\mathrm{d}x_{\mathrm{PD}}, \\ F_i^{\mathrm{TH}}(x_i) = \dfrac{Y_i b_{\mathrm{PnC}} h_{\mathrm{PnC}}^3}{12}\dfrac{\mathrm{d}^3W_i^{\mathrm{TH}}(x_i)}{\mathrm{d}x_i^3}, \end{cases} \tag{24}$$

where the superscript 'TH' is the abbreviation of time-harmonic analysis. The 4×4 matrix $\boldsymbol{CM}^{\mathrm{BS}}$ that is used in the previous subsection (band-structure analysis) is updated into a 5×5 matrix $\boldsymbol{CM}^{\mathrm{TH}}$ to consider the electroelastic coupling nature in this subsection (time-harmonic analysis). Here, $\boldsymbol{CM}^{\mathrm{TH}}$ presents the relationship between $(W(x)\ S(x)\ M(x)\ F(x)\ V(\omega))^{\mathrm{T}}$ and $(o\ p\ q\ r\ V(\omega))^{\mathrm{T}}$. At the left and right ends of each structure, the matrices $\boldsymbol{CM}_{\mathrm{PD,L}}^{\mathrm{TH}}$, $\boldsymbol{CM}_{\mathrm{PD,R}}^{\mathrm{TH}}$, $\boldsymbol{CM}_{i,\mathrm{L}}^{\mathrm{TH}}$, and $\boldsymbol{CM}_{i,\mathrm{R}}^{\mathrm{TH}}$ are expressed as

$$\begin{cases} \boldsymbol{CM}_{\mathrm{PD,L}}^{\mathrm{TH}} = \begin{pmatrix} \boldsymbol{CM}_{\mathrm{PD,L}}^{\mathrm{BS}} & \boldsymbol{PV}_{\mathrm{PD,L}} \\ \boldsymbol{0}_{1\times 4} & \boldsymbol{I}_{1\times 1} \end{pmatrix}, \\ \boldsymbol{CM}_{\mathrm{PD,R}}^{\mathrm{TH}} = \begin{pmatrix} \boldsymbol{CM}_{\mathrm{PD,R}}^{\mathrm{BS}} & \boldsymbol{PV}_{\mathrm{PD,R}} \\ \boldsymbol{0}_{1\times 4} & \boldsymbol{I}_{1\times 1} \end{pmatrix}, \\ \boldsymbol{CM}_{i,\mathrm{L}}^{\mathrm{TH}} = \begin{pmatrix} \boldsymbol{CM}_{i,\mathrm{L}}^{\mathrm{BS}} & \boldsymbol{0}_{4\times 1} \\ \boldsymbol{0}_{1\times 4} & \boldsymbol{I}_{1\times 1} \end{pmatrix}, \\ \boldsymbol{CM}_{i,\mathrm{R}}^{\mathrm{TH}} = \begin{pmatrix} \boldsymbol{CM}_{i,\mathrm{R}}^{\mathrm{BS}} & \boldsymbol{0}_{4\times 1} \\ \boldsymbol{0}_{1\times 4} & \boldsymbol{I}_{1\times 1} \end{pmatrix}, \end{cases} \tag{25}$$

where $\boldsymbol{PV}_{\mathrm{PD,L}}$ and $\boldsymbol{PV}_{\mathrm{PD,R}}$ are the 4×1 vectors that represent the relationship between the electroelastic-coupling-related terms in $(W(x)\ S(x)\ M(x)\ F(x))^{\mathrm{T}}$ and the input voltage $V(\omega)$. All components in the vectors $\boldsymbol{PV}_{\mathrm{PD,L}}$ and $\boldsymbol{PV}_{\mathrm{PD,R}}$ are associated with the non-homogeneous solution in Eqs. (13) and (24). They are expressed in terms of the electroelastic coupling coefficient ϑ_{P}. In a similar manner, the 5×5 matrix $\boldsymbol{TM}^{\mathrm{TH}}$ is defined, which determines the relationship between $(W(x)\ S(x)\ M(x)\ F(x)\ V(\omega))^{\mathrm{T}}$ given at the left and right ends of the structures. For example, the matrices $\boldsymbol{TM}_{\mathrm{PD}}^{\mathrm{TH}}$ and $\boldsymbol{TM}_i^{\mathrm{TH}}$ are expressed as

$$\begin{cases} \boldsymbol{TM}_{\mathrm{PD}}^{\mathrm{TH}} = \boldsymbol{CM}_{\mathrm{PD,R}}^{\mathrm{TH}}(\boldsymbol{CM}_{\mathrm{PD,L}}^{\mathrm{TH}})^{-1}, \\ \boldsymbol{TM}_i^{\mathrm{TH}} = \boldsymbol{CM}_{i,\mathrm{R}}^{\mathrm{TH}}(\boldsymbol{CM}_{i,\mathrm{L}}^{\mathrm{TH}})^{-1}. \end{cases} \tag{26}$$

Recall that two semi-infinite structures are adhered; one at each end of the PnC. The transverse displacement field within each semi-infinite structure is expressed as

$$\begin{cases} W_{\mathrm{SL}}^{\mathrm{TH}}(x_{\mathrm{SL}}) = o_{\mathrm{SL}}O(k_{\mathrm{SL}}x_{\mathrm{SL}}) + p_{\mathrm{SL}}P(k_{\mathrm{SL}}x_{\mathrm{SL}}) + q_{\mathrm{SL}}Q(k_{\mathrm{SL}}x_{\mathrm{SL}}) + r_{\mathrm{SL}}R(k_{\mathrm{SL}}x_{\mathrm{SL}}), \\ W_{\mathrm{SR}}^{\mathrm{TH}}(x_{\mathrm{SR}}) = o_{\mathrm{SR}}O(k_{\mathrm{SR}}x_{\mathrm{SR}}) + p_{\mathrm{SR}}P(k_{\mathrm{SR}}x_{\mathrm{SR}}) + q_{\mathrm{SR}}Q(k_{\mathrm{SR}}x_{\mathrm{SR}}) + r_{\mathrm{SR}}R(k_{\mathrm{SR}}x_{\mathrm{SR}}), \end{cases} \tag{27}$$

where $x_{\mathrm{SL}} \leqslant 0$ and $x_{\mathrm{SR}} \geqslant 0$. The zero values of x_{SL} and x_{SR} indicate the junctions between the PnC and semi-infinite structures. Here, a 5×5 scattering matrix $\boldsymbol{SM}^{\mathrm{TH}}$ is defined, which transforms $(o_{\mathrm{PD}}\ p_{\mathrm{PD}}\ q_{\mathrm{PD}}\ r_{\mathrm{PD}}\ V(\omega))^{\mathrm{T}}$ of the piezoelectric defect to $(o_{\mathrm{SL}}\ p_{\mathrm{SL}}\ q_{\mathrm{SL}}\ r_{\mathrm{SL}}\ V(\omega))^{\mathrm{T}}$ (or $(o_{\mathrm{SR}}\ p_{\mathrm{SR}}\ q_{\mathrm{SR}}\ r_{\mathrm{SR}}\ V(\omega))^{\mathrm{T}}$) of the left (or right) semi-infinite structure. Thanks to the continuity assumption, the matrices $\boldsymbol{SM}_{\mathrm{L}}^{\mathrm{TH}}$ and $\boldsymbol{SM}_{\mathrm{R}}^{\mathrm{TH}}$ are expressed as

$$\begin{cases} \boldsymbol{SM}_{\mathrm{L}}^{\mathrm{TH}} = (\boldsymbol{CM}_{\mathrm{SL},x_{\mathrm{SL}}=0}^{\mathrm{TH}})^{-1}(\boldsymbol{TM}_{\mathrm{UD}}^{\mathrm{TH}}\boldsymbol{TM}_{\mathrm{UL}}^{\mathrm{TH}})^{1-H}\boldsymbol{CM}_{\mathrm{PD,L}}^{\mathrm{TH}}, \\ \boldsymbol{SM}_{\mathrm{R}}^{\mathrm{TH}} = (\boldsymbol{CM}_{\mathrm{SR},x_{\mathrm{SR}}=0}^{\mathrm{TH}})^{-1}(\boldsymbol{TM}_{\mathrm{UD}}^{\mathrm{TH}}\boldsymbol{TM}_{\mathrm{UL}}^{\mathrm{TH}})^{N-H}\boldsymbol{TM}_{\mathrm{UD}}^{\mathrm{TH}}\boldsymbol{CM}_{\mathrm{PD,R}}^{\mathrm{TH}}. \end{cases} \tag{28}$$

One important thing to note here is that the functions $O(kx)$, $P(kx)$, $Q(kx)$, and $R(kx)$ in Eq. (15) are useful in the differentiation or integration processes; however, they lose knowledge about the propagating and attenuating directions. These characteristics motivate the modification of these four functions into $\exp(\mathrm{j}kx)$, $\exp(-\mathrm{j}kx)$, $\exp(-kx)$, and $\exp(kx)$ as

$$\begin{pmatrix} \exp(\mathrm{j}kx) \\ \exp(-\mathrm{j}kx) \\ \exp(-kx) \\ \exp(kx) \\ V(\omega) \end{pmatrix} = \begin{pmatrix} 1 & \mathrm{j} & -1 & -\mathrm{j} & 0 \\ 1 & -\mathrm{j} & -1 & \mathrm{j} & 0 \\ 1 & -1 & 1 & -1 & 0 \\ 1 & 1 & 1 & 1 & 0 \\ 0 & 0 & 0 & 0 & 1 \end{pmatrix} \begin{pmatrix} O(kx) \\ P(kx) \\ Q(kx) \\ R(kx) \\ V(\omega) \end{pmatrix} = \boldsymbol{FM} \begin{pmatrix} O(kx) \\ P(kx) \\ Q(kx) \\ R(kx) \\ V(\omega) \end{pmatrix}. \tag{29}$$

The displacement coefficients of the functions $\exp(\mathrm{j}kx)$, $\exp(-\mathrm{j}kx)$, $\exp(-kx)$, and $\exp(kx)$ are denoted as α_{Prop}, β_{Prop}, α_{Evan}, and β_{Evan}, respectively. The subscripts 'Prop' and 'Evan' represent the propagating and evanescent waves, respectively. The symbols α and β are related to the left- and right-going waves, respectively. The employment of the transforming matrix $\boldsymbol{FM}$ modifies the scattering matrices $\boldsymbol{SM}_{\mathrm{L}}^{\mathrm{TH}}$ and $\boldsymbol{SM}_{\mathrm{R}}^{\mathrm{TH}}$ in Eq. (28) into $\boldsymbol{SM}_{\mathrm{L}}^{\mathrm{TH*}}$ and $\boldsymbol{SM}_{\mathrm{R}}^{\mathrm{TH*}}$, respectively, which connect $(\alpha_{\mathrm{Prop}}\ \beta_{\mathrm{Prop}}\ \alpha_{\mathrm{Evan}}\ \beta_{\mathrm{Evan}}\ V(\omega))^{\mathrm{T}}$ of the piezoelectric defect with $(\alpha_{\mathrm{SL,Prop}}\ \beta_{\mathrm{SL,Prop}}\ \alpha_{\mathrm{SL,Evan}}\ \beta_{\mathrm{SL,Evan}}\ V(\omega))^{\mathrm{T}}$ (or $(\alpha_{\mathrm{SR,Prop}}\ \beta_{\mathrm{SR,Prop}}\ \alpha_{\mathrm{SR,Evan}}\ \beta_{\mathrm{SR,Evan}}\ V(\omega))^{\mathrm{T}}$) of the left (or right) semi-infinite structure. They are expressed as

$$\begin{cases} \boldsymbol{SM}_{\mathrm{L}}^{\mathrm{TH*}} = (\boldsymbol{FM}^{\mathrm{T}})^{-1}\boldsymbol{SM}_{\mathrm{L}}^{\mathrm{TH}}\boldsymbol{FM}^{\mathrm{T}}, \\ \boldsymbol{SM}_{\mathrm{R}}^{\mathrm{TH*}} = (\boldsymbol{FM}^{\mathrm{T}})^{-1}\boldsymbol{SM}_{\mathrm{R}}^{\mathrm{TH}}\boldsymbol{FM}^{\mathrm{T}}. \end{cases} \tag{30}$$

Here, the semi-infinite setting results in the existence of only left-going waves in the left-ended semi-infinite structure and of only right-going waves in the right-ended semi-infinite structure. In other words $\alpha_{\mathrm{SL,Prop}}$, $\alpha_{\mathrm{SL,Evan}}$, $\beta_{\mathrm{SL,Prop}}$, and $\beta_{\mathrm{SL,Evan}}$ become zero. Using this information, the vector $(\alpha_{\mathrm{PD,Prop}}\ \beta_{\mathrm{PD,Prop}}\ \alpha_{\mathrm{PD,Evan}}\ \beta_{\mathrm{PD,Evan}})^{\mathrm{T}}$ of the piezoelectric defect can be expressed, which is proportional to the input voltage $V(\omega)$ as

$$\begin{pmatrix} \alpha_{\mathrm{PD,Prop}} \\ \beta_{\mathrm{PD,Prop}} \\ \alpha_{\mathrm{PD,Prop}} \\ \beta_{\mathrm{PD,Prop}} \end{pmatrix} = - \begin{pmatrix} \boldsymbol{SM}_{\mathrm{L}}^{\mathrm{TH*}}(1,1) & \cdots & \boldsymbol{SM}_{\mathrm{L}}^{\mathrm{TH*}}(1,4) \\ \boldsymbol{SM}_{\mathrm{L}}^{\mathrm{TH*}}(3,1) & \cdots & \boldsymbol{SM}_{\mathrm{L}}^{\mathrm{TH*}}(3,4) \\ \boldsymbol{SM}_{\mathrm{R}}^{\mathrm{TH*}}(2,1) & \cdots & \boldsymbol{SM}_{\mathrm{R}}^{\mathrm{TH*}}(2,4) \\ \boldsymbol{SM}_{\mathrm{R}}^{\mathrm{TH*}}(4,1) & \cdots & \boldsymbol{SM}_{\mathrm{R}}^{\mathrm{TH*}}(4,4) \end{pmatrix}^{-1} \begin{pmatrix} \boldsymbol{SM}_{\mathrm{L}}^{\mathrm{TH*}}(1,5) \\ \boldsymbol{SM}_{\mathrm{L}}^{\mathrm{TH*}}(3,5) \\ \boldsymbol{SM}_{\mathrm{R}}^{\mathrm{TH*}}(2,5) \\ \boldsymbol{SM}_{\mathrm{R}}^{\mathrm{TH*}}(4,5) \end{pmatrix} V(\omega). \tag{31}$$

Then, the remaining displacement coefficients $\beta_{\mathrm{SL,Prop}}$, $\beta_{\mathrm{SL,Evan}}$, $\alpha_{\mathrm{SL,Prop}}$, and $\alpha_{\mathrm{SL,Evan}}$ can be obtained by

$$\begin{pmatrix} \beta_{\mathrm{SL,Prop}} \\ \beta_{\mathrm{SL,Evan}} \\ \alpha_{\mathrm{SR,Prop}} \\ \alpha_{\mathrm{SR,Evan}} \end{pmatrix} = \begin{pmatrix} \boldsymbol{SM}_{\mathrm{L}}^{\mathrm{TH*}}(2,1) & \cdots & \boldsymbol{SM}_{\mathrm{L}}^{\mathrm{TH*}}(2,4) \\ \boldsymbol{SM}_{\mathrm{L}}^{\mathrm{TH*}}(4,1) & \cdots & \boldsymbol{SM}_{\mathrm{L}}^{\mathrm{TH*}}(4,4) \\ \boldsymbol{SM}_{\mathrm{R}}^{\mathrm{TH*}}(1,1) & \cdots & \boldsymbol{SM}_{\mathrm{R}}^{\mathrm{TH*}}(1,4) \\ \boldsymbol{SM}_{\mathrm{R}}^{\mathrm{TH*}}(3,1) & \cdots & \boldsymbol{SM}_{\mathrm{R}}^{\mathrm{TH*}}(3,4) \end{pmatrix} \begin{pmatrix} \alpha_{\mathrm{PD,Prop}} \\ \beta_{\mathrm{PD,Prop}} \\ \alpha_{\mathrm{PD,Prop}} \\ \beta_{\mathrm{PD,Prop}} \end{pmatrix} + \begin{pmatrix} \boldsymbol{SM}_{\mathrm{L}}^{\mathrm{TH*}}(2,5) \\ \boldsymbol{SM}_{\mathrm{L}}^{\mathrm{TH*}}(4,5) \\ \boldsymbol{SM}_{\mathrm{R}}^{\mathrm{TH*}}(1,5) \\ \boldsymbol{SM}_{\mathrm{R}}^{\mathrm{TH*}}(3,5) \end{pmatrix} V(\omega). \tag{32}$$

It should be noted that evanescent waves become negligible when the traveling distance away from the PnC is sufficiently large. Therefore, the transverse displacement amplitudes of the generated outgoing refer to the absolute values of $\beta_{\mathrm{SL,Prop}}$ and $\alpha_{\mathrm{SL,Prop}}$, respectively. Finally, the velocity amplitudes can be calculated by using $\mathrm{j}\omega|\beta_{\mathrm{SL,Prop}}|$ and $\mathrm{j}\omega|\alpha_{\mathrm{SR,Prop}}|$, respectively. In addition, $\boldsymbol{FM}^{\mathrm{T}}(\alpha_{\mathrm{PD,Prop}}\ \beta_{\mathrm{PD,Prop}}\ \alpha_{\mathrm{PD,Evan}}\ \beta_{\mathrm{PD,Evan}}\ V(\omega))^{\mathrm{T}}$ that is given by Eqs. (29) and (31) provides $(o_{\mathrm{PD}}\ p_{\mathrm{PD}}\ q_{\mathrm{PD}}\ r_{\mathrm{PD}}\ V(\omega))^{\mathrm{T}}$. The back-substitution of this vector into Eq. (16) quantifies the generated electric current, specifically, its amplitude and phase.

4 Numerical validation through the finite element method

4.1 Planning for evaluation

Light and dark gray beams consist of magnesium and lead, respectively. The bimorph piezoelectric patches consist of PZT-5H (lead zirconate titanate, $\mathrm{Pb}(\mathrm{Zr}_x\mathrm{Ti}_{1-x}\mathrm{O}_3)$); this piezoelectric material has been widely used in sensing and actuating systems[52, 53]. Their mechanical or electrical properties are listed in Table 1. The reference of these values is the datasheet that is stored in one commercial finite-element-based software package, COMSOL Multiphysics 6.1. In addition, the geometric dimensions of the piezoelectric-defect-introduced PnC are listed in Table 2. The arrangement of eight unit cells comprises the defect-free PnC ($N = 8$); the fifth unit cell is selected for defect imposition ($H = 5$). Here, it needs to mention that this setting puts the flexural-wave-generation system in a geometrically axisymmetric state. Therefore, this case study equalizes the velocity amplitudes of two outgoing waves traveling in opposite directions through different semi-infinite structures. If generalized, the system is structurally symmetric when the defect is located at $H = N/2 + 1$ for an even number of N. Otherwise, the velocity amplitudes of the two outgoing waves are different. This issue is to be presented in Section 5.

Table 1 Material properties of structures used in a flexural-wave-generation system

Magnesium	Density	1 740 kg/m^3
	Young's modulus	43 GPa
Lead	Density	11 300 kg/m^3
	Young's modulus	17 GPa
PZT-5H	Density	7 500 kg/m^3
	1-axial elastic modulus	60.60 GPa
	3-axial dielectric permittivity	25.55 nF/m
	Piezoelectric coupling coefficient	-16.60 C/m^2

Table 2 Geometric dimensions of a piezoelectric-defect-introduced PnC

Parameter	Value
Length of the light gray beam, d_{UL}	10 mm
Length of the dark gray beam, d_{UD}	10 mm
Length of the piezoelectric defect, d_{PD}	30 mm
Height of the PnC, h_{PnC}	1 mm
Height of the piezoelectric patch, h_{P}	0.25 mm
Width, w_{PnC}	5 mm

As was done in many prior studies that deal with analytical or semi-analytical models, a comparison with the finite element method is used to validate the effectiveness of the proposed model. This work adopts COMSOL Multiphysics 6.1, which has been widely used to predict the output performance of elastic wave-propagation systems or smart-material-incorporated systems. The primary settings in this software are as follows. Commonly, two-dimensional space with the plane-stress condition is used. In the 'Eigenfrequency' setting, the 'Solid Mechanics' module with the 'Periodic Condition (type: Floquet Periodicity)' performs the band-structure

analysis (Subsections 3.2 and 4.2). As mentioned at the beginning of Subsection 3.2, only the piezoelectric-defect-introduced PnC is considered. In the 'Frequency Domain' setting, the 'Solid Mechanics' and 'Electrostatics' modules with the activation of the 'Multiphysics (Piezoelectric Effects)' module perform the time-harmonic analysis (Subsections 3.3, 4.3, and Section 5). Here, both the semi-infinite structures and the PnC are considered. The 'Perfectly Matched Layer' setting that is imposed in the outer domains away from the PnC mimics the semi-infinite conditions of each side of the wave-generation system. A unit input voltage is successfully applied through the use of 'Piezoelectric Material', 'Charge Conservation, Piezoelectric', 'Ground', and 'Terminal'. Recall that the base vector in each material coordinate of the top and bottom patches is set to lie in opposite directions along the 3-axis. The quadratic serendipity is used for the discretization of displacement fields and electric potential. The maximum size of the meshes is set to one-twentieth of the lattice constant after the convergence test. A detailed description in Refs. [27] and [28] will be helpful in understanding the COMSOL settings.

4.2 Prediction results from band-structure analysis

Figure 2(a) shows the band-structure results at the unit-cell level that are given by the first equations in Eqs. (22) and (23). The normalized Bloch wavenumber on the x-axis ranges from zero to π, and the frequency on the y-axis ranges from zero to 35 kHz. Brown-solid and green-dashed lines stand for the calculation results that are determined by the analytical and numerical models, respectively. Unlike the case of longitudinal waves, the form of a 4×4 transfer matrix provides four band structures. In this context, the analytical model stipulates three phononic band gaps (light gray-colored boxes) as (i) (1.58 kHz, 3.36 kHz), (ii) (8.16 kHz, 12.03 kHz), and (iii) (22.12 kHz, 22.66 kHz). On the other hand, the finite-element-based model determines the band gaps as (i) (1.58 kHz, 3.34 kHz), (ii) (8.04 kHz, 11.77 kHz), and (iii) (21.14 kHz, 21.91 kHz). In Fig. 2(a), as the frequency increases, the band-structure results from the analytical model tend to be larger than those from the numerical model even though the slenderness ratios of beams exceed 10. This investigation is analogous to previous studies of PnCs under flexural waves[54–56]. This similarity comes from the fact that shear deformation and rotary inertia, which are completely neglected in the Euler-Bernoulli beam theory, become significant over the high-frequency range. Indeed, if the frequency exceeds 10 kHz, the wavelength of the lead (dark gray beam) is only a few millimeters. If the sizes of the structure and the wavelength become similar in this way, shear effects or rotational inertia effects cannot be ignored anymore. Hence, prior research on phononic band-gap generation under flexural waves has demonstrated that the results of finite element method and Euler-Bernoulli beam-theory-based analytical models align well with respect to the first band gap, i.e., the gap between the first and second branches. Given this information, it is reasonable to expect that the proposed analytical model can be available for the frequency region corresponding to the first band gap. With this reason, the remaining physical quantities of interest are predicted, focusing on the frequency range near the first phononic band gap. Note that the consideration of the Timoshenko beam theory in the modeling process can alleviate this limitation. This point will be explained in Section 6.

In the circumstance of the imposition of the piezoelectric defect into the periodic unit cells, Fig. 2(b) presents the band-structure results at the PnC level that are given by the second equations in Eqs. (22) and (23). The normalized wavenumber on the x-axis is the same as in Fig. 2(a); however, the frequency on the y-axis focuses on the range from zero to 8 kHz. In each model, one defect band of flatness is newly created within the first phononic band gap. One red-solid line, ranging from 2.47 kHz to 2.49 kHz, and one blue-dashed line, ranging from 2.46 kHz to 2.48 kHz, stand for the results from the analytical and numerical models, respectively. Each defect band manifests a very narrow frequency range, and it is known that the energy-transport velocity approaches zero. The center frequency of the defect band is called the defect-band frequency. The values of the defect-band frequencies confirm that the proposed analytical model possesses high predictive capabilities. The root mean squared error (RMSE) between the defect bands determined by two different models is 0.01 kHz. It is worth pointing

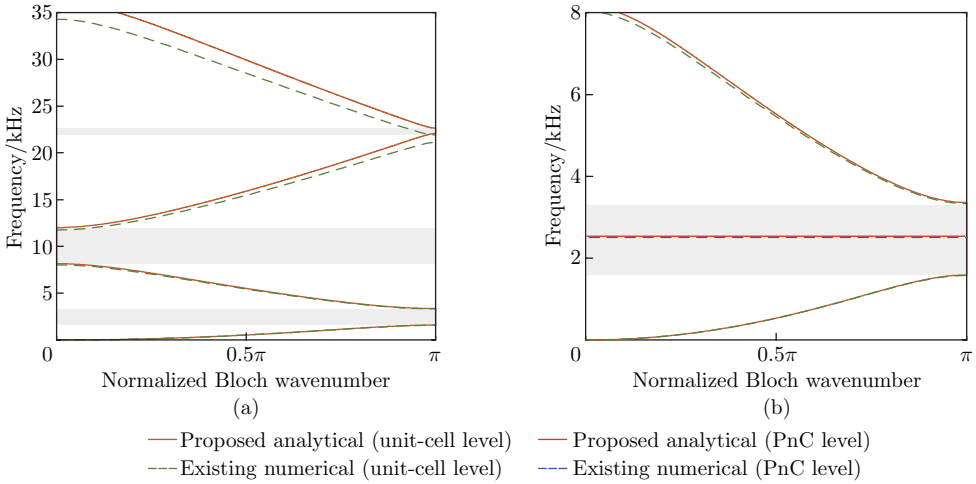

Fig. 2 Comparison results in terms of dispersion relationships (eigenvalues): (a) the creation of three phononic band gaps at the unit cell level and (b) the generation of one defect band within the first phononic band gap at the piezoelectric-defect-introduced PnC level (color online)

out that the analytical method is significantly efficient in terms of time consumption. In detail, the analytical model takes less than 1 s to obtain Fig. 2, while the finite element model requires more than 7 min.

At the center frequency of each defect band in the analytical and numerical models, Fig. 3 presents the transverse displacement field of the piezoelectric-defect-introduced PnC. Recall that this refers to the defect-mode shape. The space on the x-axis ranges from zero to 180 mm, and the normalized transverse displacement on the y-axis ranges from -1.5 to 1.5. The position of 95 mm is the center of the piezoelectric defect. Note that the transverse displacement values themselves are meaningless since they come from eigenvalue problems. Therefore, dividing the displacement field by its maximum value executes normalization. Dashed lines with red and blue colors stand for the calculation results that are determined by the analytical and numerical models, respectively. From Fig. 3, three key points need to be highlighted. First, the defect-mode shape confirms that the proposed analytical model possesses high predictive capabilities. The RMSE between the defect-mode shapes is 0.02. Second, the piezoelectric defect manifests

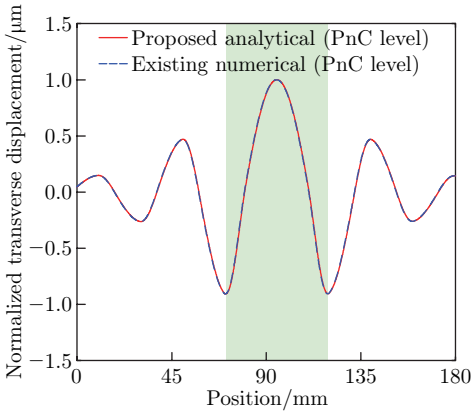

Fig. 3 Comparison results in terms of the defect-mode shape (eigenvectors) at the defect-band frequency (color online)

the markedly amplified displacement field, known as defect-mode-enabled energy localization, despite its frequency within the phononic band gap. Last, the slopes of the displacement field concerning the space have different signs at the left and right ends of the piezoelectric defect. This result indirectly implies that this defect-mode shape is suitable for flexural-wave-generation systems since the electroelastic coupling term in Eq. (9) does not vanish. The previous work on longitudinal-wave-generation when a particular defect-mode shape induces charge cancellation supports this investigation[25].

4.3 Prediction results from time-harmonic analysis

Figures 4 and 5 present the frequency response functions (FRFs) for two physical quantities of interest under a unit input voltage: (i) the velocity amplitude that is calculated by Eq. (32) (see Fig. 4), and (ii) the amplitude and phase of the generated electric current that are calculated by Eqs. (16), (29), and (31) (see Fig. 5). In all figures, for the considered piezoelectric-defect-introduced PnC, the red-solid and blue-dashed lines stand for the calculation results of the analytical and numerical models, respectively. At the same time, the comparison group consists of one wave-generation system with bimorph piezoelectric patches that are attached to an infinite structure without the defect-introduced PnC in Fig. 4. These patches have the same specification and configurations as those used in this work. A black-dashed line represents its numerical result. Inspired by the characteristics of geometrical, axial symmetry, we focus only on the waves propagating in the left, semi-infinite structure in this subsection. The frequency on the x-axis ranges from zero to 5 kHz, which includes the first phononic band gap. In Fig. 4, the logarithm-scaled velocity amplitude on y-axis lies in the range of $[10^{-1}\,\mathrm{mm/s},\ 10^{2}\,\mathrm{mm/s}]$. In Figs. 5(a) and 5(b), the amplitude and phase of the electric current on the y-axis lie in the ranges of $[10^{-4}\,\mathrm{mA},\ 10^{0}\,\mathrm{mA}]$ and $[-\pi\ \mathrm{rad},\ \pi\ \mathrm{rad}]$, respectively. The frequency spacing of both models is identically set to 10 Hz. As a side note, defect-free PnCs do not show any particular energy localization and amplification phenomena; therefore, this case is not considered in the comparison group.

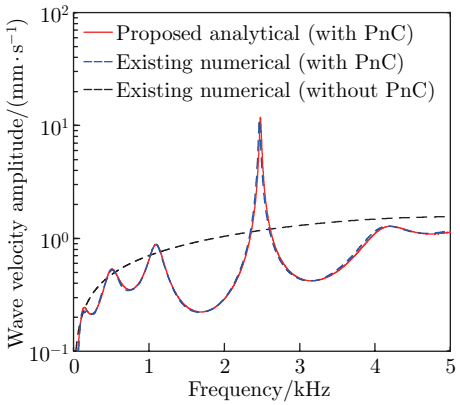

Fig. 4 Comparison results in terms of the FRF for the velocity amplitude of generated flexural waves that propagate in the left, semi-infinite structure (color online)

Similar to the band-structure analysis described in Subsection 4.2, the proposed analytical model has the ability to predict the wave-generation performance of the velocity amplitude and electric current with high accuracy; these accuracies are similar to those of the finite-element-based model. The relative error falls in a sufficiently acceptable range, despite the observation of a slight difference over the high frequencies in the given range. The RMSE between the peak frequencies is 0.01 kHz. Without matching the peak frequency, the RMSEs between the physical quantities in Figs. 4 and 5 are calculated as 0.36 mm/s, 0.02 mA, and 0.09 rad, respectively.

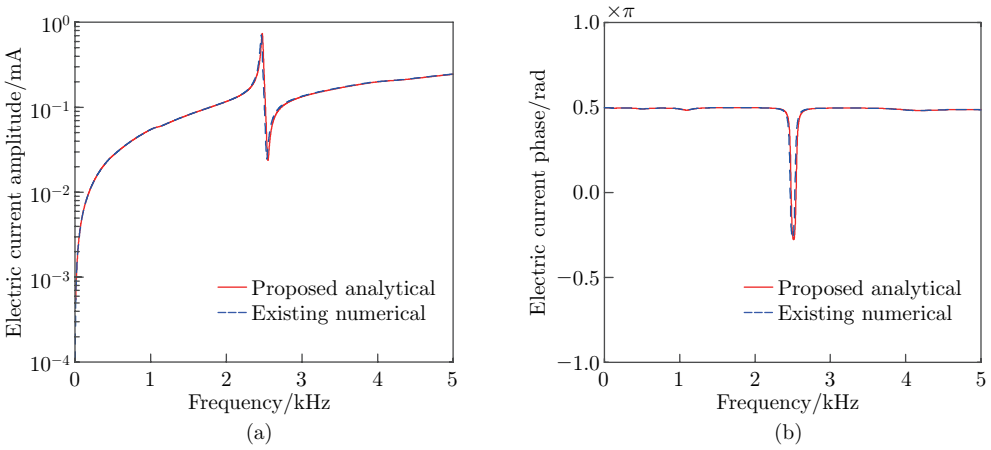

Fig. 5 Comparison results in terms of the FRF for the electric current generated by the bimorph piezoelectric patches: (a) amplitude and (b) phase (color online)

With matching the peak frequency, the RMSEs between the physical quantities are calculated as 0.02 mm/s, 0.002 mA, and 0.01 rad, respectively. It is worth pointing out that the proposed analytical method takes less than 1 s to perform the time-harmonic analysis; in contrast, the finite element model requires nearly 6 min.

Figure 4 presents one peak frequency corresponding to 2.48 kHz in the proposed analytical model. This peak frequency matches the central frequency of the defect band that is calculated in Fig. 2(b). Moreover, the velocity amplitudes of the outgoing generated waves are amplified up to ten times at each peak frequency, compared with the case in the absence of the PnC. This is a notable performance improvement. This result infers that the amplification of flexural-wave-generation performance originates from the energy-localization nature of the piezoelectric-defect-introduced PnC. To support this statement, Fig. 6 depicts the displacement fields (the so-called operating deflection shape) in the region that contains both the whole PnC and the outer semi-infinite structures at the peak frequency of 2.48 kHz in the analytical model. The information about the colors is the same as that described for Figs. 4 and 5. The left end of the PnC is set as the origin to retain consistency with Fig. 3. Since the operating deflection shape of the piezoelectric-defect-introduced PnC in the time-harmonic analysis coincides with its defect-mode shape in the band-structure analysis, it confirms the effectiveness of energy-localized behaviors of PnCs in flexural-wave-generation systems. Note that the RMSE between the operating deflection shapes is 0.02 μm.

The proposed analytical model shown in Fig. 5(a) shows two frequencies, 2.48 kHz and 2.53 kHz, which correspond to the peak and dip values of the amplitude of the electric current, respectively. What should be noted here is that the observations are well analogous to the typical characteristics that are found in resonance-type piezoelectric actuators. For example, the peak frequency in Fig. 5(a) is equal to the peak frequency in Fig. 4, which maximizes the velocity amplitude. At the same time, the phase of the electric current in Fig. 5(b) also changes rapidly by π rad. In a similar manner, the dip frequency in Fig. 5(a) is in agreement with the other frequency, at which the phase of the electric current in Fig. 5(b) changes by π rad. However, this dip frequency does not show special features in Fig. 4. The peak and dip frequencies are called the resonance and anti-resonance frequencies of the wave-generation system, respectively. The existing study in Ref. [11] which reveals the physical analogy between the defect-mode-induced energy localization and mechanical resonance strengthens the conclusion that these results are sufficiently reasonable. As a side note, the information about the

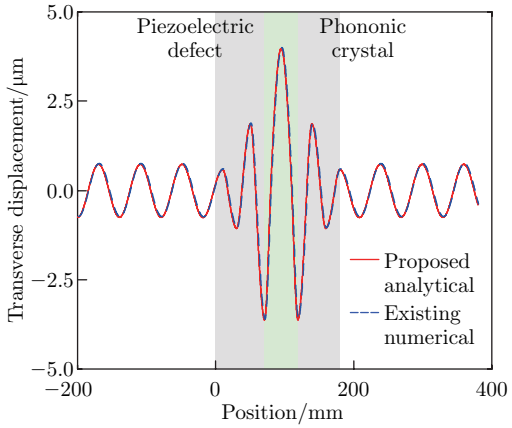

Fig. 6 Comparison results in terms of the operating deflection shape at each peak frequency in Fig. 4 (color online)

generated electric current is crucial in amplifying the velocity amplitudes of generated flexural waves from the viewpoint of electrical impedance matching. Hence, a follow-up study of the electrical engineering aspects of this method will be explained in Section 6.

5 Effects of the defect location on wave-generation performance

This section delineates how the defect location governs the velocity amplitudes of the generated flexural waves. To retain compatibility with Section 4, all values of the geometric dimensions and material properties remain fixed for the unit cells, defect, and bimorph piezoelectric patches. In addition, the number of unit cells is the same: eight ($N = 8$). Here, a parametric study is performed while sequentially changing the unit-cell location H to which the piezoelectric defect is applied from the first to the last location (i.e., $H \in \{1, 2, \cdots, 8\}$).

Remember that the setting of $H = 5$ makes the system structurally axisymmetric and provokes identical wave-generation performance in the left- and right-sided, semi-infinite structures. In contrast, the remaining defect locations will show different output performances. With this supposition, Fig. 7 displays the two velocity-amplitude FRFs that are obtained from the left and right domains as dashed lines, in red and blue colors, respectively. Figures 7(a)–7(h) are the results, respectively, when $H = 1, 2, \cdots, 8$. Note that the results given by the numerical model are not provided in this section, since the high predictive capabilities of the proposed analytical model were already confirmed in Section 4.

The velocity-amplitude FRF in red (or blue) at the left (or right), semi-infinite structure when $H = 4$ (see Fig. 7(d)), 3 (see Fig. 7(c)), and 2 (see Fig. 7(b)) is exactly equal to that in blue (or red) at the right (or left), semi-infinite structure when $H = 6$ (see Fig. 7(f)), 7 (see Fig. 7(g)), and 8 (see Fig. 7(h)), respectively. These results can be explained by the fact that the structural appearance of the system seen from the front when $H = 6$, 7, and 8 matches that seen from the rear when $N = 4$, 3, and 2, respectively. In general, the imposition of the piezoelectric defect to the Hth unit cell can be systemically equivalent to that of the $(N + 2 - H)$th unit cell for an even number of N.

When the defect is positioned at $H = 1$ (see Fig. 7(a)), 2 (see Fig. 7(b)), and 8 (see Fig. 7(h)), which are close to the ends of the PnC, the defect-band-related peak frequency is not displayed. This means that no defect-mode-enabled energy localization occurs. In the case of $H = 1$, one can intuitively imagine that defect imposition and patch attachment are done outside of the PnC. Thus, the term 'defect' does not fit in this location. In the cases of $H = 2$ and 8, the band-

gap phenomenon does not take place virtually on the piezoelectric defect's left (when $H = 2$) or right (when $H = 8$) side, despite the existence of one unit cell; this is unlike the previous case since the mechanism of band-gap formation is the periodic array of unit cells. Hence, aided by the absence of physically effective defect modes, the piezoelectric-defect-introduced PnCs with corresponding defect locations can be concluded to be unsuitable for application to flexural-wave-generation systems.

In contrast, the defect locations of $H = 3$ (see Fig. 7(c)), 4 (see Fig. 7(d)), 5 (see Fig. 7(e)), 6 (see Fig. 7(f)), and 7 (see Fig. 7(g)) represent one peak frequency of 2.47 kHz in each FRF. This means that the peak frequency is robust to the defect location if the unit cells surrounding the piezoelectric defect are arranged in sufficient numbers. This significant characteristic solidifies the effectiveness of PnC-integrated flexural-wave-generation systems. Instead, the velocity amplitude at each peak frequency depends on the defect location. When $H = 5$, a value of 11.5 mm/s is obtained for both sides. When $H = 4$, the semi-infinite structures on the left and right sides present velocity amplitudes of 11.0 mm/s and 3.60 mm/s, respectively. When $H = 3$, each structure presents 7.05 mm/s and 0.67 mm/s, respectively. Note that the periodicity weakens as the defect location becomes farther from the center (here, $H = 5$) of the system. Keeping this in mind, two observations can be summarized as follows. One is that the wave-generation performance is inevitably reduced since the incident velocity amplitude of evanescent waves

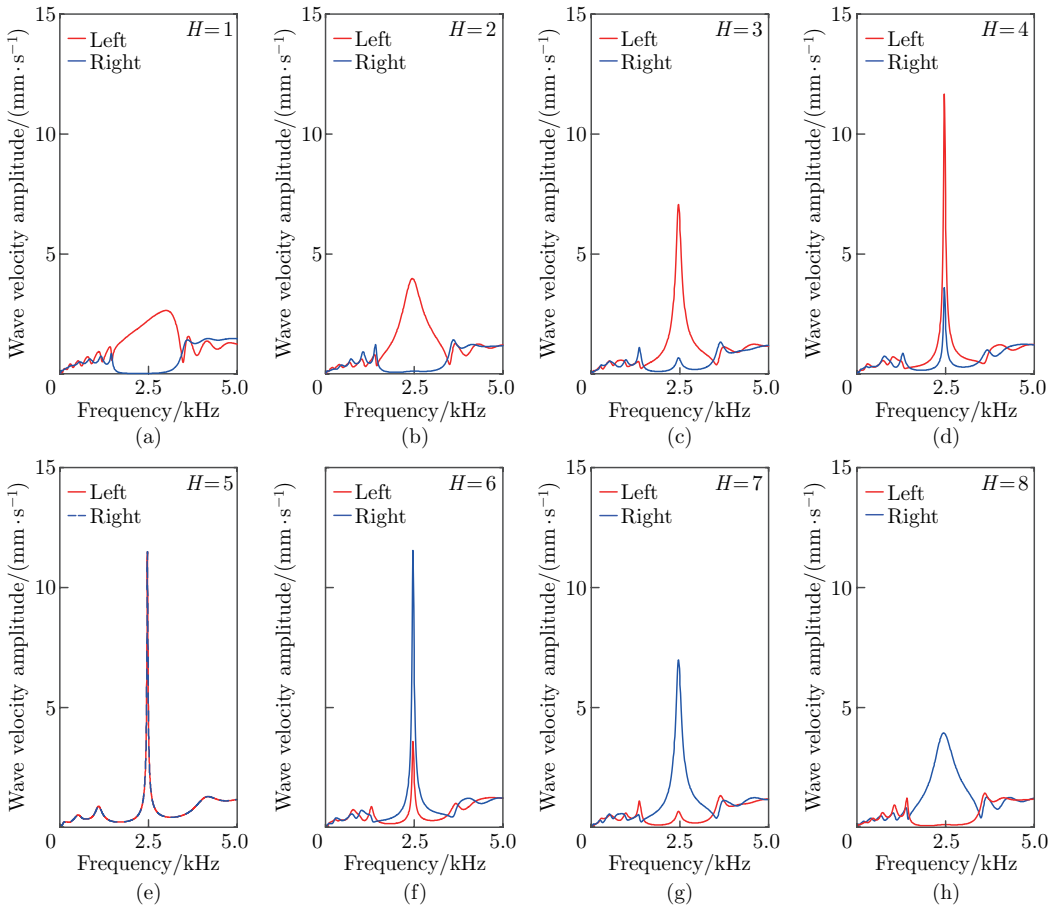

Fig. 7 Defect-location effects on the velocity amplitudes of generated flexural waves at the left- and right-sided, semi-infinite structures: (a) $H = 1$, (b) $H = 2$, (c) $H = 3$, (d) $H = 4$, (e) $H = 5$, (f) $H = 6$, (g) $H = 7$, and (h) $H = 8$ (color online)

that are transferred to a semi-infinite structure becomes smaller as they get farther from the defect. On the other hand, the incident velocity amplitude of evanescent waves, transferred to a semi-infinite structure, becomes larger as they become closer to the defect. Therefore, the trade-off relationship between an increased velocity amplitude of the evanescent waves and a weakened periodicity may result in either (i) a monotonic decrease in the velocity amplitude (in this case study) or (ii) an increasing velocity amplitude up to a certain location and a decreasing velocity amplitude thereafter. Therefore, it is necessary to select the optimal defect location in advance (during the design stage) that maximizes the velocity amplitude according to the intended use of the structure.

6 Conclusions

This study is the first attempt to contribute to improving the performance enhancement of flexural-wave-generation systems by using an energy-localization feature, an unorthodox phenomenon observed in defect-introduced PnCs. Starting from the basis of the Euler-Bernoulli beam theory, the analytical approaches based on the transfer-matrix and S-parameter methods enabled the prediction of defect bands, defect-mode shapes within phononic band gaps, and the velocity amplitudes of the finally generated flexural waves and electric current (i.e., its amplitude and phase) generated by the piezoelectric patches. In both band-structure and time-harmonic analyses, the predictive capability of the proposed analytical model is confirmed through comparison with the finite element method, using a case study with manufacturable materials and geometric values. In a case study, the root means square errors of the defect band, defect-mode shape, three FRFs for the velocity amplitude, electric current amplitude, and electric current phase are 0.01 kHz, 0.007, 0.36 mm/s, 0.02 mA, and 0.09 rad, respectively. In addition, it should be emphasized that the amplification ratio of velocity amplitudes of outgoing generated waves reach up to ten times at the defect-band frequency of 2.48 kHz, compared with the case in the absence of the PnC. Despite this high accuracy, the nature of the analytical model allows all computations to be performed in a period of seconds.

The fast-computing analytical model suggested can be applied during the design phase of piezoelectric actuators or sensors that exploit defect-introduced PnCs. These devices have various engineering applications, such as nondestructive testing to estimate the initiation and propagation of cracks for structural health monitoring, fault detection through acoustic emission testing in rotating machinery, and medical imaging through ultrasonic technology. Potential follow-up studies to this work can be organized into three primary categories to accelerate further research on building a solid bridge between defect-introduced PnCs and wave-generation systems. First, there is a need to improve the analytical model by incorporating the Timoshenko beam theory into current model-development procedures to broaden its engineering applicability in high frequencies. Second, modifications to the proposed analytical model can be explored to consider delamination effects that may result from unwanted manufacturing errors or fatigue loading during operation and result in worsening the flexural-wave-generation performance. Last, optimizing the structures and electric circuits of the piezoelectric-defect-introduced PnCs is necessary to maximize the flexural-wave-generation performance at the target frequency.

Conflict of interest The authors declare no conflict of interest.

Acknowledgements The authors would like to acknowledge the support of Dongguk University Research Fund of 2023.

References

[1] OUDICH, M., GERALD, N. J., DENG, Y., and JING, Y. Tailoring structure-borne sound through bandgap engineering in phononic crystals and metamaterials: a comprehensive review. *Advanced*

Functional Materials, **33**(2), 2206309 (2023)

[2] KENNEDY, J. and LIM, C. W. Machine learning and deep learning in phononic crystals and metamaterials: a review. *Materials Today Communications*, **33**, 104606 (2022)

[3] LEE, G., LEE, D., PARK, J., JANG, Y., KIM, M., and RHO, J. Piezoelectric energy harvesting using mechanical metamaterials and phononic crystals. *Communications Physics*, **5**(1), 94 (2022)

[4] LI, W., MENG, F., CHEN, Y., LI, Y. F., and HUANG, X. Topology optimization of photonic and phononic crystals and metamaterials: a review. *Advanced Theory and Simulations*, **2**(7), 1900017 (2019)

[5] JO, S. H. and YOUN, B. D. Longitudinal wave localization using a one-dimensional phononic crystal with differently patterned double defects. *International Journal of Mechanical Sciences*, **237**, 107783 (2023)

[6] JIN, J., HU, N. D., and HU, H. P. Size effects on the mixed modes and defect modes for a nanoscale phononic crystal slab. *Applied Mathematics and Mechanics* (*English Edition*), **44**(1), 21–34 (2023) https://doi.org/10.1007/s10483-023-2945-6

[7] MEHANEY, A. and ELSAYED, H. A. Hydrostatic pressure effects on a one-dimensional defective phononic crystal comprising a polymer material. *Solid State Communications*, **322**, 114054 (2020)

[8] ZHANG, X., LI, Y., WANG, Y., JIA, Z., and LUO, Y. Narrow-band filter design of phononic crystals with periodic point defects via topology optimization. *International Journal of Mechanical Sciences*, **212**, 106829 (2021)

[9] HE, F. Y., SHI, Z. Y., QIAN, D. H., LU, Y. K., XIANG, Y. J., and FENG, X. L. Flexural wave bandgap properties of phononic crystal beams with interval parameters. *Applied Mathematics and Mechanics* (*English Edition*), **44**(2), 173–188 (2023) https://doi.org/10.1007/s10483-023-2947-8

[10] JIANG, S., DAI, L. X., CHEN, H., HU, H. P., JIANG, W., and CHEN, X. D. Folding beam-type piezoelectric phononic crystal with low-frequency and broad band gap. *Applied Mathematics and Mechanics* (*English Edition*), **38**(3), 411–422 (2017) https://doi.org/10.1007/s10483-017-2171-7

[11] JO, S. H., YOON, H., SHIN, Y. C., and YOUN, B. D. Revealing defect-mode-enabled energy localization mechanisms of a one-dimensional phononic crystal. *International Journal of Mechanical Sciences*, **215**, 106950 (2022)

[12] YAN, W., ZHANG, G., and GAO, Y. Investigation on the tunability of the band structure of two-dimensional magnetorheological elastomers phononic crystals plate. *Journal of Magnetism and Magnetic Materials*, **544**, 168704 (2022)

[13] DENG, T., ZHANG, S., and GAO, Y. A magnetic-dependent vibration energy harvester based on the tunable point defect in 2D magneto-elastic phononic crystals. *Crystals*, **9**(5), 261 (2019)

[14] WU, L. Y., WU, M. L., and CHEN, L. W. The narrow pass band filter of tunable 1D phononic crystals with a dielectric elastomer layer. *Smart Materials and Structures*, **18**(1), 015011 (2008)

[15] ARRANGOIZ-ARRIOLA, P., WOLLACK, E. A., PECHAL, M., and WITMER, J. D. Coupling a superconducting quantum circuit to a phononic crystal defect cavity. *Physical Review X*, **8**(3), 031007 (2018)

[16] SHAKERI, A., DARBARI, S., and MORAVVEJ-FARSHI, M. K. Designing a tunable acoustic resonator based on defect modes, stimulated by selectively biased PZT rods in a 2D phononic crystal. *Ultrasonics*, **92**, 8–12 (2019)

[17] THOMES, R. L., BELI, D., and JUNIOR, C. D. M. Space-time wave localization in electromechanical metamaterial beams with programmable defects. *Mechanical Systems and Signal Processing*, **167**, 108550 (2022)

[18] TIAN, Y., ZHANG, W., TAN, Z., and CHO, C. Chiral edge states for phononic crystals based on shunted piezoelectric materials. *Extreme Mechanics Letters*, **50**, 101568 (2022)

[19] ALY, A. H., NAGATY, A., and KHALIFA, Z. Piezoelectric material and one-dimensional phononic crystal. *Surface Review and Letters*, **26**(2), 1850144 (2019)

[20] WU, Y., MA, Y., ZHENG, H., and RAMAKRISHNA, S. Piezoelectric materials for flexible and wearable electronics: a review. *Materials and Design*, **211**, 110164 (2021)

[21] JO, S. H. and YOUN, B. D. An improved analytical model that considers lateral effects of a phononic crystal with a piezoelectric defect for elastic wave energy harvesting. *International Journal of Mechanical Sciences*, **205**, 106593 (2021)

[22] HE, Z., ZHANG, G., CHEN, X., CONG, Y., GU, S., and HONG, J. Elastic wave harvesting in piezoelectric-defect-introduced phononic crystal microplates. *International Journal of Mechanical Sciences*, **239**, 107892 (2023)

[23] LYU, X. F., FANG, X., ZHANG, Z. Q., HUANG, Z. L., and CHUANG, K. C. Highly localized and efficient energy harvesting in a phononic crystal beam: defect placement and experimental validation. *Crystals*, **9**(8), 391 (2019)

[24] HOSSEINKHANI, A., EBRAHIMIAN, F., YOUNESIAN, D., and MOAYEDIZADEH, A. Defected meta-lattice structures for the enhanced localized vibrational energy harvesting. *Nano Energy*, **100**, 107488 (2022)

[25] JO, S. H. and YOUN, B. D. An explicit solution for the design of a target-frequency-customized, piezoelectric-defect-introduced phononic crystal for elastic wave energy harvesting. *Journal of Applied Physics*, **130**(18), 184902 (2021)

[26] ZHONG, J. and XIANG, J. Designing a phononic crystal with a large defect to enhance elastic wave energy localization and harvesting. *Japanese Journal of Applied Physics*, **61**(1), 017002 (2022)

[27] JO, S. H., LEE, D., YOON, H., and YOUN, B. D. Double piezoelectric defects in phononic crystals for ultrasonic transducers. *Journal of Physics D*: *Applied Physics*, **56**(7), 074002 (2023)

[28] JO, S. H. and YOUN, B. D. Enhanced ultrasonic wave generation using energy-localized behaviors of phononic crystals. *International Journal of Mechanical Sciences*, **228**, 107483 (2022)

[29] JO, S. H., SHIN, Y. C., CHOI, W., YOON, H., YOUN, B. D., and KIM, M. Double defects-induced elastic wave coupling and energy localization in a phononic crystal. *Nano Convergence*, **8**(1), 27 (2021)

[30] LUO, Y. S., YANG, S. X., LYU, X. F., CHUANG, K. C., LIU, Y., HE, J., and CHENG, Q. C. Identifying delamination in carbon fiber composites based on defect modes in imperfect phononic crystals. *Journal of Applied Physics*, **131**(5), 055109 (2022)

[31] WANG, Y., PERRAS, E., GOLUB, M. V., FOMENKO, S. I., ZHANG, C., and CHEN, W. Manipulation of the guided wave propagation in multilayered phononic plates by introducing interface delaminations. *European Journal of Mechanics-A/Solids*, **88**, 104266 (2021)

[32] ZHOU, W. and LIM, C. W. Topological edge modeling and localization of protected interface modes in 1D phononic crystals for longitudinal and bending elastic waves. *International Journal of Mechanical Sciences*, **159**, 359–372 (2019)

[33] LI, P. and BIWA, S. Flexural waves in a periodic non-uniform Euler-Bernoulli beam: analysis for arbitrary contour profiles and applications to wave control. *International Journal of Mechanical Sciences*, **188**, 105948 (2020)

[34] ERTURK, A. and INMAN, D. J. A distributed parameter electromechanical model for cantilevered piezoelectric energy harvesters. *Journal of Vibration and Acoustics*, **130**(4), 041002 (2008)

[35] WANG, G. Analysis of bimorph piezoelectric beam energy harvesters using Timoshenko and Euler-Bernoulli beam theory. *Journal of Intelligent Material Systems and Structures*, **24**(2), 226–239 (2013)

[36] ALI, A., PASHA, R. A., ELAHI, H., SHEERAZ, M. A., BIBI, S., HASSAN, Z. U., EUGENI, M., and GAUDENZI, P. Investigation of deformation in bimorph piezoelectric actuator: analytical, numerical and experimental approach. *Integrated Ferroelectrics*, **201**(1), 94–109 (2019)

[37] CHEN, N., YAN, P., and OUYANG, J. A generalized approach on bending and stress analysis of beams with piezoelectric material bonded. *Sensors and Actuators A*: *Physical*, **290**, 54–61 (2019)

[38] YI, J., WU, Z., XIA, R., and LI, Z. Reconfigurable metamaterial for asymmetric and symmetric elastic wave absorption based on exceptional point in resonant bandgap. *Applied Mathematics and Mechanics* (*English Edition*), **44**(1), 1–20 (2023) https://doi.org/10.1007/s10483-023-2949-7

[39] LI, Z., LIU, J., HU, B., WANG, Y., and SHEN, H. Wave propagation analysis of porous functionally graded piezoelectric nanoplates with a visco-Pasternak foundation. *Applied Mathematics and Mechanics* (*English Edition*), **44**(1), 35–52 (2023) https://doi.org/10.1007/s10483-023-2953-7

[40] ERTURK, A. and INMAN, D. J. An experimentally validated bimorph cantilever model for piezoelectric energy harvesting from base excitations. *Smart Materials and Structures*, **18**(2), 025009 (2009)

[41] YOON, H., YOUN, B. D., and KIM, H. S. Kirchhoff plate theory-based electromechanically-coupled analytical model considering inertia and stiffness effects of a surface-bonded piezoelectric patch. *Smart Materials and Structures*, **25**(2), 025017 (2016)

[42] MAZILU, T., DUMITRIU, M., and TUDORACHE, C. On the dynamics of interaction between a moving mass and an infinite one-dimensional elastic structure at the stability limit. *Journal of Sound and Vibration*, **330**(5), 3729–3743 (2011)

[43] NORRIS, A. N. and PACKO, P. Non-symmetric flexural wave scattering and one-way extreme absorption. *The Journal of the Acoustical Society of America*, **146**(1), 873–883 (2019)

[44] DONG, H. W., SU, X. X., WANG, Y. S., and ZHANG, C. Topological optimization of two-dimensional phononic crystals based on the finite element method and genetic algorithm. *Structural and Multidisciplinary Optimization*, **50**, 593–604 (2014)

[45] VERES, I. A., BERER, T., and MATSUDA, O. Complex band structures of two dimensional phononic crystals: analysis by the finite element method. *Journal of Applied Physics*, **114**(8), 083519 (2013)

[46] XIE, L., XIA, B., LIU, J., HUANG, G., and LEI, J. An improved fast plane wave expansion method for topology optimization of phononic crystals. *International Journal of Mechanical Sciences*, **120**, 171–181 (2017)

[47] CAO, Y., HOU, Z., and LIU, Y. Convergence problem of plane-wave expansion method for phononic crystals. *Physics Letters A*, **327**(2-3), 247–253 (2004)

[48] HAN, L., ZHANG, Y., NI, Z. Q., ZHANG, Z. M., and JIANG, L. H. A modified transfer matrix method for the study of the bending vibration band structure in phononic crystal Euler beams. *Physica B*: *Condensed Matter*, **407**(23), 4579–4583 (2012)

[49] SHU, H., LIU, W., LI, S., DONG, L., WANG, W., LIU, S., and ZHAO, D. Research on flexural wave band gap of a thin circular plate of piezoelectric radial phononic crystals. *Journal of Vibration and Control*, **22**(7), 1777–1789 (2016)

[50] JIANG, P., WANG, X. P., CHEN, T. N., and ZHU, J. Band gap and defect state engineering in a multi-stub phononic crystal plate. *Journal of Applied Physics*, **117**(15), 154301 (2015)

[51] LI, Y., CHEN, T., WANG, X., MA, T., and JIANG, P. Acoustic confinement and waveguiding in two-dimensional phononic crystals with material defect states. *Journal of Applied Physics*, **116**(2), 024904 (2014)

[52] KHAN, A., KHAN, F. R., and KIM, H. S. Electro-active paper as a flexible mechanical sensor, actuator and energy harvesting transducer: a review. *Sensors*, **18**(10), 3474 (2018)

[53] ZASZCZYNSKA, A., GRADYS, A., and SAJKIEWICZ, P. Progress in the applications of smart piezoelectric materials for medical devices. *Polymers*, **12**(11), 2754 (2020)

[54] GUO, Y., LI, L., and CHUANG, K. C. Analysis of bending waves in phononic crystal beams with defects. *Crystals*, **8**(1), 21 (2018)

[55] ZHANG, Y., NI, Z. Q., JIANG, L. H., HAN, L., and KANG, X. W. Study of the bending vibration characteristic of phononic crystals beam-foundation structures by Timoshenko beam theory. *International Journal of Modern Physics B*, **29**(20), 1550136 (2015)

[56] ZHAO, P., YUAN, L., MA, T., and WEI, H. Study on tunable band gap of flexural vibration in a phononic crystals beam with PBT. *Crystals*, **11**(11), 1346 (2021)